Engineered Protein-Iron Oxide Hybrid Biomaterial for MRI-traceable Drug Encapsulation

Journal:	*Molecular Systems Design & Engineering*
Manuscript ID	ME-ART-01-2022-000002.R1
Article Type:	Paper
Date Submitted by the Author:	14-Apr-2022
Complete List of Authors:	Hill, Lindsay; NYU Tandon School of Engineering, Chemical and Biomolecular Engineering Britton, Dustin; NYU Tandon School of Engineering, Chemical and Biomolecular Engineering Jihad, Teeba; NYU Tandon School of Engineering, Chemical and Biomolecular Engineering Punia, Kamia; NYU Tandon School of Engineering, Chemical and Biomolecular Engineering Xie, Xuan; NYU Tandon School of Engineering, Chemical and Biomolecular Engineering Delgado-Fukushima, Erika; NYU Tandon School of Engineering, Chemical and Biomolecular Engineering Liu, Che; NYU Tandon School of Engineering, Chemical and Biomolecular Engineering Mishkit, Orin; NYU Langone Health Liu, Chengliang; NYU Tandon School of Engineering, Chemical and Biomolecular Engineering Hu, Chunhua; New York University, Department of Chemistry Meleties, Michael; NYU Tandon School of Engineering, Chemical and Biomolecular Engineering Renfrew, P.; Flatiron Institute Bonneau, Richard; New York University, Wadghiri, Youssef; NYU Langone Health Montclare, Jin; NYU Tandon School of Engineering, Chemical and Biomolecular Engineering; New York University, Chemistry

Design, System, Application Statement:

We have recently designed the drug encapsulating protein, Q, by domain swapping the cartilage oligomeric matrix protein coiled-coil domain, (COMPcc), resulting in positively and negatively charged patches that allows for the protein to undergo hierarchical self-assembly into mesofibers. We have further engineered Q by utilizing residue specific incorporation of the methionine analog, azidohomoalanine (AHA) which allows for the copper-catalyzed azide-alkyne cycloaddition-click chemistry of a propargylglycine-bearing CMms6 peptide. We exploit the iron oxide templating capacity of CMms6 to generate a hybrid iron oxide biomaterial, Q_{AHA}-X-CMms6•USPIO, which is detectable via T_2/T_2^* weighted MRI. We show that the protein is capable of encapsulation and release of the chemotherapeutic small molecule, doxorubicin, and by linking the protein to MRI-detectable USPIOs we greatly improve the T_2^* sensitivity at 7-T compared to the standard agent, Feraheme, likely due to a high density of USPIO templated onto the mesofiber scaffold. The protein scaffold is generated using acidic conditions and chemical crosslinking to stabilize the mesoscale fibers and doxorubicin encapsulation. Additionally, USPIOs are typical of USPIOs produced in similar CMms6 peptide templation. The large scale, encapsulation and imaging capability of this biomaterial makes it a good candidate for potential application as a theranostic tissue-engineered scaffold.

Engineered Protein-Iron Oxide Hybrid Biomaterial for MRI-traceable Drug Encapsulation

Lindsay K. Hill[†,‡,§,¶,¤], Dustin Britton[†,¤], Teeba Jihad[†], Kamia Punia, Xuan Xie[†], Erika Delgado-Fukushima[†], Che Fu Liu[†], Orin, Mishkit[§,¶], Chengliang Liu[†], Chunhua Hu[∇], Michael Meleties[†], P. Douglas Renfrew[‖], Richard Bonneau[‖,⊥,#], Youssef Z. Wadghiri[§,¶], and Jin Kim Montclare[†,¶,∇,°]*

†. Department of Chemical and Biomolecular Engineering, New York University Tandon School of Engineering, Brooklyn, New York, 11201, USA
‡. Department of Biomedical Engineering, SUNY Downstate Medical Center, Brooklyn, New York, 11203, USA
§.Center for Advanced Imaging Innovation and Research (CAI^{2}R), New York University School of Medicine, New York, New York, 10016, USA
¶.Bernard and Irene Schwartz Center for Biomedical Imaging, Department of Radiology, New York University School of Medicine, New York, New York, 10016, USA
‖. Center for Computational Biology, Flatiron Institute, Simons Foundation, New York, New York, 10010, USA
⊥. Center for Genomics and Systems Biology, New York University, New York, New York, 10003, USA
#. Courant Institute of Mathematical Sciences, Computer Science Department, New York University, New York, New York, 10009, USA
∇. Department of Chemistry, New York University, New York, New York, 10012, USA
°. Department of Biomaterials, New York University College of Dentistry, New York, New York, 10010, USA
¤ Equal contribution
* Corresponding author
Email: Montclare@nyu.edu
Add Orin Mishkit *i*[§,¶] and ORCID

ABSTRACT

Labeled protein-based biomaterials have become a popular for various biomedical applications such as tissue-engineered, therapeutic, or diagnostic scaffolds. Labeling of protein biomaterials, including with ultrasmall super-paramagnetic iron oxide (USPIO) nanoparticles, has enabled a wide variety of imaging techniques. These USPIO-based biomaterials are widely studied in magnetic resonance imaging (MRI), thermotherapy, and magnetically-driven drug delivery which provide a method for direct and non-invasive monitoring of implants or drug delivery agents. Where most developments have been made using polymers or collagen hydrogels, shown here is the use of a rationally designed protein as the building block for a meso-scale fiber. While USPIOs have been chemically conjugated to antibodies, glycoproteins, and tissue-engineered scaffolds for targeting or improved biocompatibility and stability, these constructs have predominantly served as diagnostic agents and often involve harsh conditions for USPIO synthesis. Here, we present an engineered protein-iron oxide hybrid material comprised of an azide-functionalized coiled-coil protein with small molecule binding capacity conjugated via bioorthogonal azide-alkyne cycloaddition to an alkyne-bearing iron oxide templating peptide, CMms6, for USPIO biomineralization under mild conditions. The coiled-coil protein, dubbed Q, has been previously shown to form nanofibers and, upon small molecule binding, further assembles into mesofibers via encapsulation and aggregation. The resulting hybrid material is capable of doxorubicin encapsulation as well as sensitive T_2*-weighted MRI darkening for strong imaging capability that is uniquely derived from a coiled-coil protein.

KEYWORDS

protein engineering, biomineralization, fiber, iron oxide, drug encapsulation, MRI

INTRODUCTION

Hybrid organic-inorganic biomaterials have been used in therapeutic, diagnostic, and tissue-engineered scaffolds [1]. Specifically, using a hybrid biomaterial for tissue-engineered scaffolds enables functionalization of an implant for applications such as drug delivery and imaging [2]. Engineered biomaterials pose several advantages for all biomedical applications for including biocompatibility, biodegradability, and low toxicity [3]. Of increasing popularity are those that also incorporate imaging moieties [4]. Much of this work includes nanoparticle-based biomaterials made of either superparamagnetic iron-based metal oxide nanoparticles (SPIOs) or ultrasmall superparamagnetic iron oxide (USPIO) particles, gold nanoparticles, polymer-based nanoparticles [5], and magnetoferritin nanoparticles [6] that have imaging capabilities and further functionalization properties. Beyond nanoparticles, popular materials also include collagen and various other natural and synthetic polymers that provide the dual benefit of biocompatibility and the ability to incorporate diagnostic agents including USPIOs [5, 7-9].

(U)SPIOs have been utilized preclinically and clinically predominantly as transverse relaxation time (T_2/T_2*)-shortening, or negative-contrast, magnetic resonance imaging (MRI) agents. These agents impart localized darkening on images [10] with additional utility in hyperthermic therapy [11], cell tracking [12-14], and magnetically-driven drug delivery [15]. Furthermore, these constructs are typically comprised of protein conjugated to USPIOs that have either been purchased commercially [16] or previously synthesized under harsh conditions [17, 18]. By contrast, biomineralization exploits organic biomolecules or biomimetics to serve as templates for controlled crystal formation under mild, even ambient, conditions [19]. In the case of iron oxide, magnetotactic bacteria such as *Magnetospirillum magneticum* [20] biomineralize uniform magnetite (Fe_3O_4) nanoparticles within magnetosome organelles [21-23]. Magnetosome-associated proteins, perhaps most commonly magnetite biomineralization protein Mms6, serve as

templates for magnetite nanoparticle nucleation and growth, controlling the resulting crystal size and morphology [20]. The acidic C-terminus of Mms6, or CMms6, is rich in metal-binding hydroxyl and carboxyl groups [20, 24] and can independently organize iron oxide nanoparticles under mild conditions via partial oxidation and co-precipitation reactions [22]. The use of CMms6 as a biomimetic material for USPIO biomineralization could be advantageous over traditional synthesis techniques, particularly for biomedical applications that favor milder aqueous conditions.

In the last thirty years, advances in synthetic and chemical biology [25], including in non-canonical amino acid (NCAA) incorporation [26, 27] and bioorthogonal conjugation strategies [26], have popularized studies of NCAA-derived proteins. Specifically, NCAAs bearing azide moieties have enabled conjugation to alkyne-bearing molecules of interest through azide-alkyne [3 + 2] cycloaddition, coined “click” chemistry [28]. Such reactions allow for conjugation with high specificity and yield with minimal byproducts [29]. Here, we explore bioorthogonal azide-alkyne [3 + 2] click chemistry to conjugate the CMms6 peptide to a drug-encapsulating protein in order to engineer an MRI-traceable protein-USPIO hybrid biomaterial.

We’ve recently engineered the protein Q by domain swapping the cartilage oligomeric matrix protein coiled-coil domain (COMPcc), resulting in positively and negatively charged surface patches [30]. Under acidic conditions, these patches direct protein assembly through electrostatic interactions into robust nanofibers with diameters tens to hundreds of nanometers wide [30, 31]. When bound to the small molecule curcumin, Q protein nanofibers further assembled into mesoscale fibers with dimensions comparable to those of natural-occurring α-keratin, collagen, and spider silk [1], but with the benefit of small molecule binding [1, 30]. Given Q’s ability to generate mesofibers, a scale uncommonly reported in protein-based fiber fabrication,

it was chosen to be further engineered in this work. Larger fiber diameters have resulted in slower drug release kinetics likely due to the longer path length of diffusion [32], which is a desired property for a sustainable drug delivery vehicle. Residue-specific incorporation of the methionine analog, azidohomoalanine (AHA) [33, 34], was employed herein to synthesize an azide-functionalized Q protein, Q_{AHA}. Using copper-catalyzed azide-alkyne cycloaddition-click chemistry, Q_{AHA} was conjugated to a synthetic alkyne-bearing CMms6 peptide [20]. By conjugating Q_{AHA} to a propargylglycine-bearing CMms6, we sought to exploit the iron oxide templating capacity of CMms6 in order to generate a hybrid agent that is detectable via T_2/T_2*-weighted MRI.

In addition to MRI detection, the drug binding capacity of Q_{AHA} provides the hybrid construct with therapeutic potential [1]. Here we assess the ability of Q_{AHA}, alone and conjugated to CMms6, to bind doxorubicin (Dox), an anthracycline chemotherapeutic agent that has been widely used in the treatment of various cancer types [35]. While Dox is a potent drug, it is unstable at physiological pH [36, 37] and has the unfortunate potential for off-target effects [38], both of which may be mitigated by its encapsulation within a delivery vehicle [38]. This protein-USPIO hybrid biomaterial, therefore, aims to integrate the drug binding potential of the Q protein with the capacity of CMms6 to synthesize uniform USPIOs, creating an MRI-detectable mesofiber. This work will guide further exploration of protein-based biomaterial engineering, taking advantage of the vast potential beyond their use in targeting and nanoparticle coating.

EXPERIMENTAL SECTION

Materials. M15MA *E. coli* cells were a gift from David Tirrell (California Institute of Technology) [33]. Bacto-tryptone, sodium chloride, yeast extract, tryptic soy agar, ampicillin, kanamycin, sodium phosphate monobasic monohydrate ($NaH_2PO_4 \cdot H_2O$), sodium phosphate dibasic anhydrous (Na_2HPO_4), ammonium chloride (NH_4Cl), potassium phosphate monobasic (KH_2PO_4), sodium hydroxide (NaOH), dextrose monohydrate (D-glucose), magnesium sulfate, calcium chloride ($CaCl_2$), manganese chloride tetrahydrate ($MnCl_2 \cdot 4H_2O$), cobaltous chloride hexahydrate ($CoCl_2 \cdot 6H_2O$), zinc sulfate heptahydrate ($ZnSO_4 \cdot 7H_2O$), boric acid (H_3BO_3), isopropyl β-D-1-thiogalactopyranoside (IPTG), tris hydrochloride (Tris HCl), Pierce bicinchoninic acid (BCA) assay kit, Pierce snakeskin dialysis tubing 3.5 K MWCO, sodium dodecyl sulfate, Pierce C18 tips with 10 µL bed, BD Clay Adams glass microscopy slides, bissulfosuccinimidyl suberate (BS^3), ascorbic acid, Slide-A-Lyzer MINI Dialysis devices in 3.5 kDa MWCO 2 mL, and Slide-A-Lyzer dialysis cassettes G2 in 7 kDa MWCO 3 mL were acquired from Thermo Fisher Scientific. All 20 naturally occurring amino acids, nickel (III) chloride hexahydrate ($NiCl_2 \cdot 6H_2O$), sodium molybdate dihydrate ($Na_2MoO_4 \cdot 2H_2O$), iron (III) chloride ($FeCl_3$), iron (II) chloride tetrahydrate ($FeCl_2 \cdot 4\ H_2O$), thiamine hydrochloride (vitamin B), ProteoMass peptide and protein MALDI-MS calibration kit, copper (II) sulfate pentahydrate ($CuSO_4 \cdot 5H_2O$), TraceCERT® iron standard for ICP, hydroxylamine hydrochloride sodium acetate, and 1,10-phenanthroline, low gelling temperature agarose, and dimethylsulfoxide (DMSO) were purchased from Sigma Aldrich. Copper (II) chloride anhydrous ($CuCl_2$), sodium selenite (Na_2SeO_3), imidazole, and Nitric Acid ACS reagent 70% were purchased from Acros Organics. Hydrochloric acid (HCl) and Coomassie® Brilliant Blue G-250 were purchased from VWR. HiTrap immobilized metal affinity chromatography (IMAC) fast flow (FF) 5 mL column for protein purification and Whatman™

filter paper for transmission electron microscopy sample preparation were purchased from Cytiva Life Sciences. Macrosep and Microsep Advance Centrifugal Devices 3K MWCO and 0.2 μm syringe filters were purchased from PALL. Acrylamide/bis solution (30%) 29:1 and natural polypeptide SDS-PAGE standard were purchased from Bio-Rad. Doxorubicin free base (95%) was purchased from MedKoo Biosciences. Tris(3-hydroxypropyltriazolylmethyl)amine (THPTA) and azidohomoalanine (AHA) were purchased from Click Chemistry. Propargylglycine-CMms6 (prg-CMms6) peptide was synthesized *via* solid phase peptide synthesis by LifeTein, LLC. Formvar/carbon-coated copper grids (FCF400-Cu) and 1% uranyl acetate for transmission electron microscopy were purchased from Electron Microscopy Sciences. Feraheme® (ferumoxytol injection) was from AMAG Pharmaceuticals, Inc. Borosilicate glass disposable culture tubes (6 mm x 50 mm) were purchased from Kimble-Chase.

Modeling of Q-Dox Binding. Dox conformer libraries were generated using the BioChemical Library ConformerGenerator application [39]. Docking between the Q protein and Dox was performed using Rosetta software with the ligand transform protocol [40]. The docking protocol was used to simultaneously sample ligand conformations, while allowing for flexibility in both the side chains and backbone of the protein. Due to the long, narrow axial pore of the Q protein, five independent runs were conducted where the starting position of Dox was adjusted to scale the full length of the cavity. 500 models were generated from each starting conformation for a total of 2,500 models.

Protein Expression. Wild-type Q (Q_{WT}) and Q_{AHA} were expressed in chemically-competent M15MA *E. coli* cells [33]. An aliquot of 100 μL M15MA cells, carrying the kanamycin-resistant

Qiagen pREP4 plasmid [41], was transformed *via* heat shock using 250 ng of ampicillin-resistant pQE30/Q plasmid [30] maintaining an N-terminal 6x histidine tag (6x His-tag). Transformed cells were recovered in Lysogeny Broth and grown at 37ºC and 300 rpm for 45 min. Cells were then plated onto tryptic soy agar plates supplemented with ampicillin (0.2 mg mL^{-1}) and kanamycin (0.035 mg mL^{-1}). Colonies were grown at 37ºC for 16 hr. Single colonies were used to inoculate starter cultures prepared in modified M9 medium (0.5 M Na_2HPO_4, 0.22 M KH_2PO_4, 0.08 M NaCl, and 0.18 M NH_4Cl) containing all 20 natural amino acids (100 µg mL^{-1}), ampicillin (0.2 mg mL^{-1}), kanamycin (0.035 mg mL^{-1}), vitamin B (0.034 mg mL^{-1}), D-glucose (0.1 mg mL^{-1}), magnesium sulfate (0.22 mg mL^{-1}), calcium chloride (0.01 mg mL^{-1}), and trace metals (0.02% v/v). The trace metal solution was prepared by combining 40 mM $CaCl_2$, 20 mM $MnCl_2 \bullet 4H_2O$, 4 mM $CoCl_2 \bullet 6H_2O$, 20 mM $ZnSO_4 \bullet 7H_2O$, 4 mM $CuCl_2$, 4 mM $NiCl_2 \bullet 6H_2O$, 4 mM Na_2SeO_3, 4 mM H_3BO_3, and 4 mM $Na_2MoO_4 \bullet 2H_2O$ with 100 mM $FeCl_3$ in 120 mM HCl. Starter cultures were incubated at 37ºC and 350 rpm for 16 hr. Starter cultures were subsequently added to 400 mL or 200 mL M9 medium for Q_{WT} or Q_{AHA} expression, respectively, at 4% (v/v) and supplemented as described above. Expression flasks were incubated at 37ºC and 350 rpm until the optical density at 600 nm (OD_{600}) was 0.7-0.9. At this OD_{600}, Q_{WT} expression was induced with IPTG (200 µg mL^{-1}) and returned to 37ºC to shake at 350 rpm for 3 hr. Following 3 hr expression, cells were pelleted at 4ºC and 5,000 rpm for 20 min and stored at -80ºC until purification. For Q_{AHA} expression, at an OD_{600} of 0.7-0.9, cells were pelleted at 4ºC and 4,000 x g for 20 min. Pellets were then washed four times in succession by resuspending in ice cold 0.9% NaCl in order to remove the 20 canonical amino acid supplemented M9 expression media. Washed pellets were resuspended in supplemented M9 containing 19 natural amino acids (100 µg mL^{-1}), excluding methionine, and grown at 37ºC and 350 rpm for 15 min to deplete residual methionine. Q_{AHA}

expression was then induced with the addition of azidohomoalanine (AHA) (100 μg mL^{-1}) [33] and IPTG (200 μg mL^{-1}). Induced cells were grown at 37ºC and 350 rpm for 3 hr and then pelleted at 4ºC and 4,000 x g for 20 min prior to storage at -80ºC. Aliquots of 1 mL cell culture were obtained before and 3 hr post-induction for assessment of protein expression *via* 12% sodium dodecyl sulfate polyacrylamide gel electrophoresis (SDS-PAGE).

Protein Purification. Q proteins were purified *via* immobilized metal affinity chromatography (IMAC) under denaturing conditions. Cell pellets were thawed and resuspended in Buffer A (50 mM Tris HCl, 500 mM NaCl, 6 M urea, pH 8.0) at one-tenth the expression volume. Suspensions were placed in an ice bath and lysed *via* ultrasonic probe sonication (Q500 sonicator, QSonica) at 45% amplitude, pulse 5 seconds on and 5 seconds off, for 2 min in 1 min increments. Cellular debris was removed *via* centrifugation at 4ºC and 14,000 x g for 50 min prior to purification *via* syringe-pump driven IMAC using a cobalt-charged HiTrap IMAC FF 5 mL column. Protein was eluted using a gradient of Buffer B (50 mM Tris HCl, 500 mM NaCl, 6 M urea, 500 mM imidazole, pH 8.0) to increase imidazole concentrations from 10-500 mM. Purity of fractions was assessed *via* 12% SDS-PAGE, stained and imaged as described above. Pure protein elutions were filtered through a 0.2 μm syringe filter and added to 3.5 kDa molecular weight cut off (MWCO) snakeskin tubing for dialysis to remove urea and imidazole under acidic conditions favorable to nanofiber assembly, as previously reported [30]. Dialysis was performed at 4ºC in 50 mM phosphate buffer (PB) pH 4.0 using a step-wise decrease in urea concentration, halving the concentration successively over three 5 L-buckets (3 M to 0.75 M urea) followed by six buckets containing 50 mM PB pH 4.0 with 0 M urea. Dialyzed proteins were concentrated using 3 kDa MWCO Macrosep and Microsep Advance centrifugal devices (Pall Corporation) at

4ºC and 2,000 x g, and the protein concentrations were determined by bicinchoninic acid (BCA) assay compared to a standard curve of known albumin concentrations.

Assessment of Azidohomoalanine Incorporation. The percentage of AHA incorporated into Q_{AHA} was assessed using matrix-assisted laser desorption/ionization-time of flight mass spectrometry (MALDI-TOF MS) on a Bruker UltrafleXtreme MALDI-TOF/TOF. Separately, 10 µg of Q_{WT} or Q_{AHA} was digested by sequencing-grade modified trypsin (0.5 µg), pre-warmed to 30ºC for 15 minutes, in 60 mM ammonium bicarbonate buffer at 37ºC and 300 rpm for 6 hr. Trypsin digestion was quenched using 10% trifluoroacetic acid (TFA) until pH 4.0 was reached. Quenched samples were subjected to zip-tip preparation using C18-packed tips wetted in 50% acetonitrile and equilibrated in 0.1% TFA. Protein was bound to the column, washed with 0.1% TFA, and eluted using 0.1% TFA in 90% acetonitrile into α-cyano-4-hydrocinnamic acid (CHCA) matrix at 1:1 protein elution:matrix volume. Samples were spotted onto a Bruker MTP 384 steel target plate and dried in a desiccation chamber. Tryptic peptide masses were determined with ExPASy tool PeptideMass[42, 43], factoring in the 5 Da difference in molecular weight between methionine and AHA. Peptide standards were combined and added 1:1 with CHCA for instrument calibration. The intensities of Q_{WT} and Q_{AHA} peaks corresponding to the tryptic peptide NTAPQM/A_{HA}LR, containing the second methionine/AHA residue, were compared to calculate AHA incorporation *via* equation (1).

$$AHA\ incorporation\ (\%) = 100\% \cdot \frac{Intensity\ of\ AHA\ peak}{Intensity\ of\ Met\ peak + Intensity\ of\ AHA\ peak} \quad (1)$$

AHA incorporation was further confirmed using amino acid analysis performed by the Molecular Structure Facility at the University of California, Davis. Purified Q_{WT}, Q_{AHA}, and AHA were

oxidized overnight in performic acid and run on a Hitachi L-8900 amino acid analyzer to measure the amount of methionine present in the samples.

Circular Dichroism. Circular Dichroism (CD) spectroscopy was performed to assess the secondary structure of Q proteins at 40 μM using a Jasco J-815 CD spectrometer with a PTC-423S single position Peltier temperature control system. Single wavelength scans were acquired from 190-250 nm at 50 nm min^{-1} with 1 nm steps at 25ºC. Thermostability studies included wavelength scans every 10ºC from 25ºC to 85ºC. The mean residue ellipticity (MRE) was calculated from ellipticity values (θ) using equation (2) [31].

$$\theta_{MRE} = \frac{\theta}{10 \cdot molarity \cdot path\ length\ (cm) \cdot number\ of\ amino\ acids} \quad (2)$$

The θ_{MRE} values at the two spectral minima, one at 222 nm (θ_{222}) and one between 200 nm-210 nm (θ_{min}), were used to estimate α-helicity by the ratio of $\theta_{222}/\theta_{min}$, where 0.8-0.9 is typically used to describe isolated α-helices and ≥1.0 suggests coiled-coil conformation [44]. The percentages of α-helicity, β-content (β-sheets and β-turns), and unordered structure were predicted with CONTIN/LL software [45-47].

Attenuated Total Reflectance-Fourier Transform Infrared Spectroscopy. Attenuated Total Reflectance-Fourier Transform Infrared (ATR-FTIR) spectroscopy was performed to confirm protein secondary structure using a Nicolet 6700 Fourier Transform Infrared Spectrometer equipped with a diamond ATR accessory and a mercury cadmium telluride (MCT)-A detector. A 5 μL sample of 40 μM protein was spotted onto the diamond surface and a 128-scan spectrum was acquired at room temperature from 4000-400 cm^{-1} with 4 cm^{-1} data spacing, following acquisition of a buffer-only background spectrum. Spectra were analyzed in PeakFit software using a second

derivative zero baseline correction and peak deconvolution with Gaussian function on the amide I region 1700-1600 cm^{-1} as previously described [30]. Peak deconvolution was complete when the goodness of fit demonstrated r^2=0.99. Areas under the peaks were calculated by PeakFit for each secondary structure [48].

Transmission Electron Microscopy. Transmission electron microscopy (TEM) was employed to assess Q nanofiber assembly at pH 4.0 as well as the morphology of subsequently synthesized iron oxide in the presence or absence of CMms6-mediated templation. Samples were spotted at 3 µL volume onto formvar/carbon-coated copper grids for 1 min at room temperature, blotted with Whatman™ filter paper, washed with 5 µL deionized water (diH_2O), and again blotted with filter paper. Protein samples in the absence of iron oxide were negatively stained with 3 µL 1% uranyl acetate for 1 min, blotted, and allowed to dry. Samples containing iron oxide were not stained. Diameters of Q_{WT} and Q_{AHA} fibers at pH 4.0 were measured using ImageJ software[48] and differences were tested for significance using an unpaired two-tailed student's *t*-test. Diameters of USPIO nanoparticles were also measured using ImageJ [49].

In addition to standard bright-field TEM, energy dispersive X-ray spectroscopy (EDS) mode was used to obtain elemental maps of USPIO-bound protein samples. Maps were acquired for 45 min to assess the location and relative intensity of carbon, nitrogen, oxygen, and iron. All TEM images were acquired at 120 kV on a JEOL JEM-1400 microscope at the Center for Functional Nanomaterials at the Brookhaven National Laboratory.

Determination of Drug Binding Ratio. To determine the optimal protein:drug ratio for binding Dox, a spectrophotometric assay was performed using Q_{WT} protein. Dox was dissolved in

DMSO. Q_{WT}, at 10 μM, was added to a 96-well solid back plate and incubated in the dark at room temperature and 300 rpm overnight for 16 hr with 0-100 μM Dox in 50 mM PB pH 7.4 containing 1% v/v DMSO. A BioTek Synergy H1 microplate reader was used to excite Dox at 490 nm and emissions were read at 600 nm. The baseline spectra of Dox, at 0-100 μM in 50 mM PB pH 7.4 containing 1% v/v DMSO, was subtracted from the fluorescence intensities (relative fluorescence units, RFUs) of Q_{WT}•Dox at corresponding concentrations. The difference in RFUs was plotted and the binding ratio at which the fluorescence nearly plateaued was used for subsequent drug binding experiments in which Dox was bound to Q proteins using 40 μM Q in 50 mM PB, pH 7.4, containing 1% v/v DMSO at the optimal binding ratio. Samples were incubated at room temperature and 300 rpm for 16 hr in the dark. Dox-bound samples studied for protein structure, *via* CD and ATR-FTIR, were first dialyzed to remove DMSO using 50 mM PB pH 8.0-filled 3.5 KDa MWCO dialysis conicals at room temperature and 300 rpm for 2 hr prior to buffer exchange and another 2 hr dialysis.

Chemical Crosslinking. After dialysis of all unbound Dox, chemical crosslinking was performed to stabilize Dox-bound fibers by adding 3 mM bis(sulfosuccinimidyl) suberate (BS^3) at room temperature and 300 rpm for 1 hr in the dark. BS^3 is reactive toward primary amines on the N-terminus and lysine residues. The reaction was quenched with 25 mM Tris HCl, pH 7.5 for 15 min and an aliquot was removed for visualization *via* fluorescence microscopy. Quenched samples were also dialyzed into 50 mM PB, pH 8.0 using 3.5 KDa MWCO dialysis conicals at 4°C and 10 x g to remove excess BS^3 crosslinker and Dox. The samples were dialyzed for 4 hrs prior to buffer exchange and subsequent overnight dialysis. Crosslinking was confirmed *via* 12% SDS-PAGE.

Fluorescence Microscopy. Dox-bound Q fiber assembly, pre- and post-BS^3 crosslinking, was assessed on a Leica DMI4000 fluorescence microscope equipped with a Leica DFC310 FX camera and an N2.1 filter. Samples were spotted on glass microscopy slides and sealed with a glass coverslip immediately prior to imaging. Differences in the diameters of Dox-bound Q_{WT} and Q_{AHA} fibers pre- and post-crosslinking were assessed for significance using a two-way analysis of variance (ANOVA) statistical test.

Copper-catalyzed Azide-Alkyne Cycloaddition Click Chemistry. Following post-crosslinking dialysis, crosslinked Q_{AHA} mesofibers were conjugated *via* copper-catalyzed azide-alkyne cycloaddition [50] to the 3 kDa CMms6 [20, 24], custom-synthesized by LifeTein, LLC. The reaction was also performed with crosslinked Q_{WT} mesofibers as a negative control. In 50 mM PB, pH 8.0, crosslinked Q_{WT} and Q_{AHA} mesofibers were separately added to CMms6 at 1:10 Q:CMms6 molar ratio in the presence of pre-incubated 1 mM $CuSO_4$•5 H_2O and 5 mM THPTA, and cycloaddition was initiated with 25 mM sodium ascorbate [51]. The reaction was incubated at room temperature and 300 rpm for 1 hr and stopped by dialysis into 50 mM PB, pH 8.0 using 7 kDa MWCO dialysis cassettes to remove excess reagents at 4ºC overnight, including three exchanges of the dialysis buffer. Pre- and post-click reaction and post-dialysis samples were assessed *via* 12% SDS-PAGE.

Cell Viability Assay. Cell viability assays were performed to assess the efficacy of free Dox and Dox delivered by crosslinked and CMms6-conjugated Q_{AHA} mesofibers (Q_{AHA}-X-CMms6) on the MCF-7 human breast adenocarcinoma cell line using the Dojindo cell counting kit-8 (CCK-8) [52, 53]. Because the drug was removed with previous dialysis steps, Q_{AHA}-X-CMms6 was rebound to Dox overnight at the pre-determined optimal binding ratio, at room

temperature and 300 rpm for 16 hr in the dark to yield Q_{AHA}-X-CMms6•Dox. MCF-7 cells were plated in black-walled clear-bottomed 96 well plates at 5,000 cells/well in 100 µL minimum essential media (MEM) supplemented with 10% fetal bovine serum, 1% penicillin/streptomycin, and 0.01 mg mL^{-1} human recombinant insulin. The cells were permitted to recover and adhere to the wells at 37°C with 5% CO_2 for 48 hr. Following incubation, MEM was removed and fresh MEM was added at 90 µL/well. The remaining 10 µL was comprised of increasing concentrations of Dox alone, Q_{AHA}-X-CMms6, Q_{AHA}-X-CMms6•Dox, or 50 mM PB pH 7.4, each with a final 0.1% v/v DMSO co-solvent, plated in triplicate. After treatment for 24 hr or 48 hr at 37°C with 5% CO_2, media was removed, wells were washed two times with 100 µL 1x phosphate buffered saline (PBS), pH 7.4, and 90 µL of fresh MEM was added. The cytotoxicity of the complexes was evaluated *via* CCK-8 assay. A 10 µL aliquot of the colorimetric tetrazolium salt WST-8, reduced by viable cells to a soluble formazan product detectable *via* absorption at 450 nm, was added to each well, mixed, and incubated at 37°C with 5% CO_2 for 3 hr. Plates were assessed spectrophotometrically. The average absorption of the baseline, cell-free wells with 50 mM PB, pH 7.4 + 0.1% v/v DMSO in MEM, was subtracted from treated cells and their viabilities were normalized to the absorption of untreated cells provided only 50 mM PB, pH 7.4 + 0.1% v/v DMSO in MEM. Three independent trials were performed. The IC_{50} values, the concentration of drug at which cell viability is reduced to 50%, were calculated for Dox and Q_{AHA}-X-CMms6•Dox in GraphPad Prism (GraphPad Software) and their differences at 24 hr and 48 hr were assessed for significance using Tukey's honestly significant difference (HSD) test for multiple pair-wise comparisons.

Iron Oxide Templation. Following post-click dialysis, USPIO templation was performed *via* co-precipitation of $FeCl_3$ and $FeCl_2$ in the presence or absence of 40 μM CMms6, crosslinked Q_{WT}, or Q_{AHA}-X-CMms6 in 50 mM PB, pH 8.0. Peptide/protein constructs were N_2-sparged and incubated at 4ºC and 300 rpm for 1 hr with N_2-sparged $FeCl_3$•6 H_2O and $FeCl_2$•4 H_2O at final concentrations of 20 mM and 10 mM, respectively [23]. After 1 hr, samples were brought to room temperature and iron oxide was precipitated upon reduction with N_2-sparged 100 mM NaOH until the final NaOH concentration reached 20-fold that of $FeCl_2$[54] and pH 9.0-10.0 was achieved. The formation of iron oxide was confirmed visually through the appearance of black precipitate [23, 55]. Magnetization of USPIOs was confirmed by sample manipulation with a neodymium magnet. Samples were washed three times with room-temperature N_2-sparged 50 mM PB, pH 8.0, and gently pelleted at room temperature for 2min at 350 x g between washes. The final iron concentration was determined using a colorimetric assay reliant on the complexation of Fe^{2+} with 1,10-phenanthroline[55]. Briefly, 25 μL of iron oxide-bound sample or iron calibration standard was digested in 1 mL 70% nitric acid at 100°C for 14 hr on a digital dry bath heater. Aliquots of 10 μL samples were evaporated at 115°C for 30 min. Subsequently, 46 μL diH_2O and 30 μL 8.06 M hydroxylamine hydrochloride were added to evaporated samples to reduce Fe^{3+} to Fe^{2+} at room temperature for 1 hr. Next, 49 μL of 1.22 M sodium acetate and 75 μL of 13 mM 1,10-phenanthroline were added. The samples' absorbance at 508 nm was acquired to calculate the iron concentration against a standard curve of known iron concentrations.

X-ray Diffraction. X-ray diffraction (XRD) was used to confirm the iron oxide composition of templated USPIOs by calculating their crystal lattice *d*-spacing. XRD angles were acquired with a Bruker Smart Apex II equipped with a PHOTON II C14 area detector and Incotec

microfocus Mo tube. Q_{AHA}-X-CMms6•USPIO samples were mounted on a MiTeGen loop using minimum immersion oil. *2Θ* scattering was collected at *2Θ* = –20° and ω = –10° in a ϕ rotation method over 300 seconds. Two-dimensional diffraction data was analyzed by DIFFRAC.EVA program [56]. The 10 most prominent peaks (by relative count) from the scattering spectra were determined using MATLAB and Statistics Toolbox Release 2017b (The Mathworks, Inc.). Crystal lattice *d*-spacing was calculated by Bragg's law using 0.71073 Å as the wavelength corresponding to the K-α radiation of the Molybdenum anode used.

Magnetic Resonance Imaging. Magnetic resonance (MR) imaging and relaxometry was acquired on a 7-Tesla (7-T) Bruker micro-MRI Avance II console interfaced to a 200 mm Magnex Scientific horizontal bore magnet equipped with a Resonance Research BGA-9S actively shielded gradient coil insert (inner diameter =90 mm, gradient strength =750 mT/m, rise time =100 μs). All phantom MR studies were acquired with a house-made circularly polarized Litz coil (29 mm length, 21.5 mm inner diameter, and 23.5 mm outer diameter). MRI phantom samples were prepared with Q_{AHA}-X-CMms6•USPIO or FDA-approved iron oxide-based Feraheme for comparison. All samples were diluted in 1.0% degassed low-melting agarose to avoid settling during image acquisition [57, 58]. A 1.0% agarose solution was prepared with heat and allowed to degas under vacuum and magnetic stirring at 300 rpm. Once cooled to 37°C, USPIO samples were mixed into 500 μL agarose aliquots to yield dilutions from 500 μM to 62.5 μM iron. 50 mM PB, pH 8.0 in agarose was included for reference. Agarose samples were added to 6 mm x 50 mm glass culture tubes and permitted to solidify. The contrast-enhancing ability of MRI agents is typically measured by the water protons longitudinal relaxivity (r_1) for their brightening ability and by the transverse relaxivities (r_2) and (r_2*) for the darkening effect in solutions containing the

paramagnetic agent at 1 mM concentration [59, 60]. However, the use of ultrahigh magnetic field (strength ≥7 Tesla), such as in the current study, tend to decrease the effective R_1 relaxation rate enhancement (thereby decreasing the brightening efficiency) and increase the R_2 and R_{2*} (corresponding to T_2 and T_{2*} shortening). This renders the darkening effect of the USPIOs examined in this study predominant [61-63]. Hence, in the current context the characterization was focused on r_2 and r_2* relaxivities [60] in order to elucidate the darkening efficiency. To this effect, all MRI protocols consisted of 2D multi-slice sequences with a 256 x 256 matrix size and 25.6 mm x 25.6 mm Field of view resulting in 100 μm x 100 μm in-plane spatial resolution with a 500 μm slice thickness and 300 μm slice gap. Transverse relaxation time T_2 values were acquired using a multi-slice multi-echo (MSME) sequence with a repetition time (TR) =20,000 ms, echo time (TE)=8.5 ms, echo spacing (ES) =8.5 ms, number of echoes (NEchoes) =64 resulting in echo times ranging from to 8.5 ms to 544 ms, flip angle (FA) =180°, acquisition bandwidth (BW) =100 KHz, number of averages (NAV) =1, number of repetition (NR) =1, and acquisition time (T_{IM}) =1 hr 25 min. -Apparent transverse relaxation time T_2* values were acquired with a multi-gradient echo (MGE) sequence with TR =500 ms, TEs =3-75.77 ms, ES =3.83 ms, Nechoes =20, FA =10°, BW =100 KHz, NAV =28, NR =1, and T_{IM} = 59 min. The signal intensity of all samples across their respective echo times was determined in ImageJ. Absolute T_2 and T_{2*} relaxation times were calculated using Origin Pro 8 software based on a nonlinear curve fitting of the signal intensities. r_2 and r_{2*} relaxivity values were calculated as the slope of the relaxation rate R_2 ($1/T_2$, s^{-1}) and R_{2*} ($1/T_{2*}$, s^{-1}), respectively relative to the concentration of iron (mM). Differences in r_2 and r_2* values between Q_{AHA}-X-CMms6•USPIO and Feraheme were assessed for significance *via* Tukey's HSD test for multiple pair-wise comparisons.

***In vivo* Magnetic Resonance Imaging.** In vivo experiments were performed on a 7-T Bruker 7030 Biospec Micro MRI system equipped with helium zero-boil-off and a nitrogen free ultra-shield refrigerated horizontal magnet (ID=300-mm). The system was interfaced to an Avance 3-HD console (Bruker Biospin, Billerica, MA, USA) operated under Paravision 6.1. The system was equipped with an actively shielded gradient coil insert (BGA-12S-HP, outer diameter=198 mm, inner diameter=114 mm) powered by high performance power gradient amplifiers (IECO, Helsinki, Finland) operating at 300 A/500 V. The combination of the amplifier with the gradient coil insert results in the following performance: gradient strength=660 mT/m; maximum linear slew rate = 4,570 T m-1s-1 and rise time = 130 μs. A circularly polarized Bruker volume MRI probe with 40-mm inner diameter and 45-mm length was used to ensure homogenous RF coverage of the whole adult mouse body.

4- to 6-week C57/BL6 mice (n= 2) were used for the *in vivo* MRI experiments. Mice were injected an identical 3-μl volume of IO nanomaterials in each hindlimb muscles to illustrate and compare the efficacy *in vivo*. The volume infusion was performed in each of the two gastrocnemius muscles with either the Q biomaterial decorated with a 12 mM biosynthesized iron or with 5-mM clinical IO nanoparticle Feraheme.

The *in vivo* testing of the T_2-weighted effect of the nanomaterials was performed in the axial orientation using a two-dimensional (2D) multi-slice spin echo (SE) sequence (repetition time TR=2500-ms, echo time TE=9.3-ms, Matrix size 256×256, field-of-view=38.4-mm×38.4-mm resulting in 150-μm in-plane resolution with 150-μm slice thickness and 150-μm slice gap) with an acquisition time less than 11-min. A 3D multi-gradient echo (GE) sequence in the coronal orientation under 150-μm isotropic resolution was also acquired in less than 25-min (TR=30-ms, minimum TE=2.7-ms, echo spacing ES=3.3-ms with effective echo ranging from 2.7-ms to 19.2-

ms, FA=15°, Matrix size 256×256×190, field-of-view=38.4-mm×38.4-mm×28.5-mm) to facilitate the comparison between both sequences. Additionally, a 3D T_1-weighted ultrashort echo time (UTE) sequence was also acquired in less than 9-min (TR=10-ms, TE=11-μs, FA=30°, Matrix size 128×128×128, field-of-view=42-mm×42-mm×42-mm resulting in 328-μm isotropic resolution with 51360 projections). The UTE sequence was chosen to help highlight the T_1-brightening effect of iron oxide particles by enabling a 11-μs echo time in order to prevent the T_2/T_2* signal loss typically encountered with conventional pulse sequences in which the minimal echo time amounts to the millisecond range.

Statistical Analysis. GraphPad Prism was utilized for all statistical analysis. Specific statistical tests used were defined above for individual experiments. Differences were deemed statistically significant when demonstrating $p < 0.05$ (*), $p < 0.01$ (**), $p < 0.001$ (***), or $p < 0.0001$ (****).

RESULTS

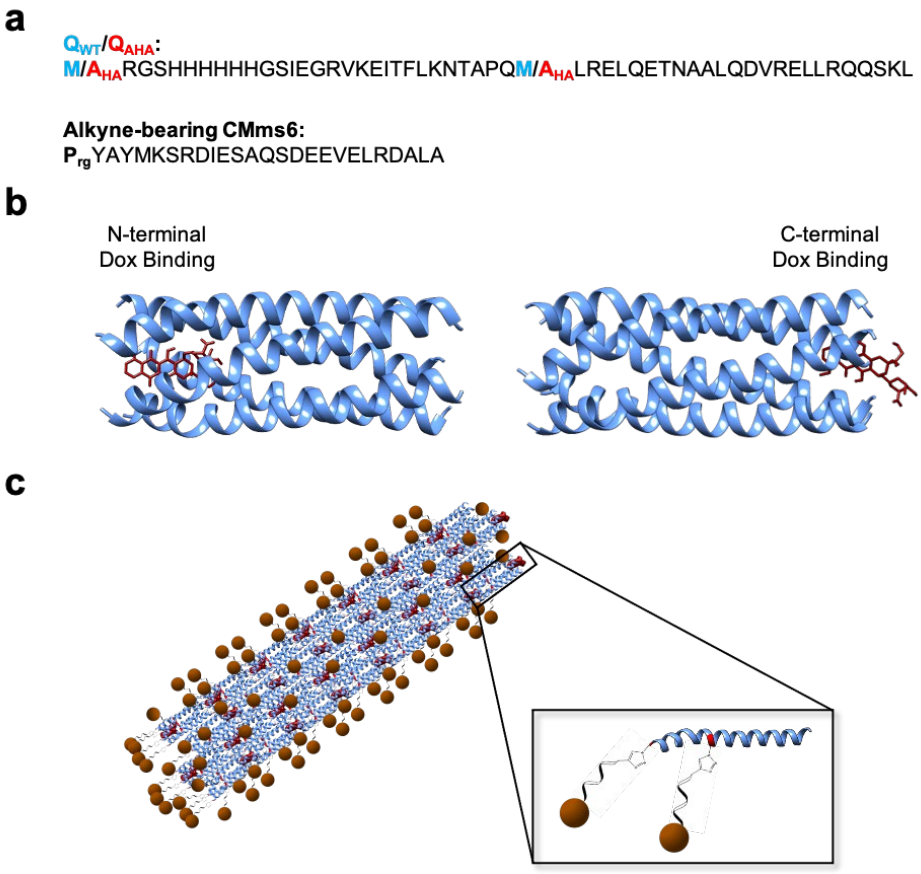

Figure 1. Schematic of protein-iron oxide hybrid biomaterial including (a) primary amino acid sequences for wild type Q_{WT}, azide-functionalized Q_{AHA}, and the prg-CMms6; (b) the two lowest-energy models from docking simulations illustrating N-terminal and C-terminal Dox binding by the Q protein; and (c) schematic of proposed protein-iron oxide hybrid biomaterial mediated through USPIO templation by CMms6. Inset illustrates the triazole ring resulting from azide-alkyne cycloaddition between Q_{AHA} and CMms6.

Hybrid Biomaterial Design and Protein Biosynthesis. We have designed a protein-iron oxide hybrid biomaterial for dual therapeutic and diagnostic (theranostic) scaffold-based

applications. Our strategy for engineering this hybrid material involves the synthesis of an azide-bearing azidohomoalanine-incorporated coiled-coil Q protein, Q_{AHA}, that maintains the capacity for drug encapsulation (**Figure 1a**). Protein modeling of Q reveals that the long, internal hydrophobic pore diameter varies along the length of the protein, with the widest part being a pentalobular void formed due to a kink induced by alanine and proline in the 27^{th} and 28^{th} residue positions, respectively. Of the 2500 possible models, the lowest-energy model predicts that Dox is able to fully bind within the large N-terminal cavity, with a total energy of -762.697 Rosetta Energy Units (REUs) (**Figure 1b**). Lowest-energy modeling also predicts that Dox participates in a variety of interactions with the polar C-terminus, without fully penetrating the hydrophobic pore, as the amino sugar and ketone moieties remain outside of the cavity; the lowest energy state resulting from C-terminal binding demonstrated -760.913 REUs (**Figure 1b**). Experimental binding of Dox by Q_{AHA} nanofibers results in mesofiber formation, which is stabilized through chemical crosslinking. Azide-alkyne cycloaddition is then performed to conjugate Q_{AHA}

mesofibers to the alkyne-bearing iron oxide-templating peptide CMms6 for subsequent USPIO templation (**Figure 1c**).

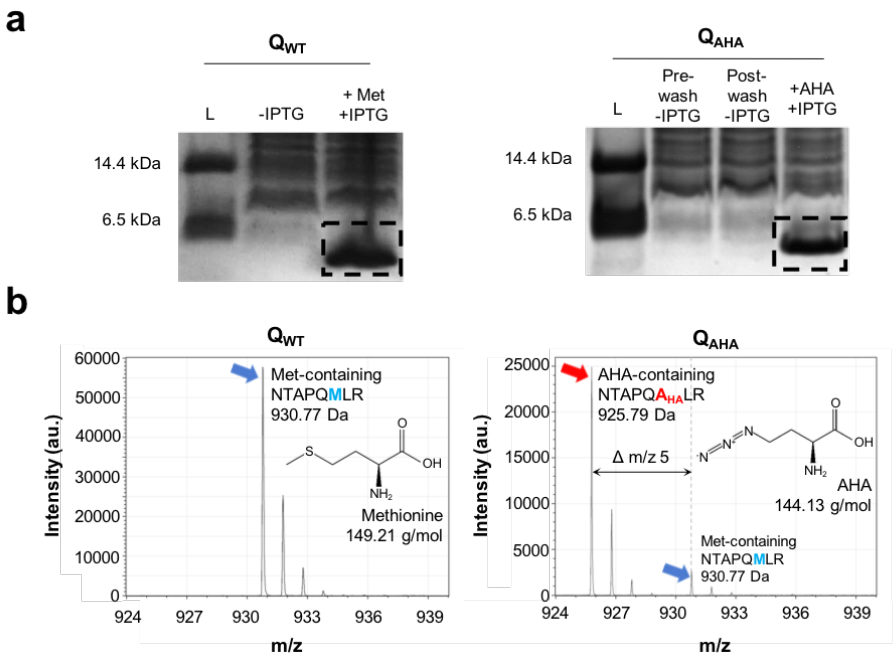

Figure 2. Biosynthesis of wild type and azide-functionalized Q proteins confirmed via (a) 12% SDS-PAGE of Q_{WT} and Q_{AHA} protein expression in M15MA *E. coli*, including ladder (L). (b) AHA incorporation was assessed by comparing MALDI-TOF MS spectra of Q_{WT} and Q_{AHA} tryptic fragment NTAPQM/A_{HA}LR containing the second Met/AHA residue.

In order to generate azide-functionalized Q_{AHA}, protein biosynthesis in the presence and absence of methionine, AHA, and IPTG was carried out in methionine auxotrophic M15MA *E. coli* [33] and assessed via 12% SDS-PAGE. Protein bands at 6.3 kDa confirmed successful over-expression of Q_{WT} and Q_{AHA} (**Figure 2a**). Following protein purification (**Figure S1, Table S1**), AHA incorporation was assessed via MALDI-TOF MS (**Figure 2b**) and amino acid analysis (AAA) (**Table S2**). As expected, the Q_{WT} peptide fragment, NTAPQMLR, was 930.77 Da and the Q_{AHA} fragment, NTAPQA_{HA}LR, was 925.79 Da, demonstrating a negative shift of 5 Da via

MALDI-TOF MS (**Figure 2b**), indicative of AHA incorporation with 88.53% ± 5.03% (*N*=6) efficiency at the second methionine residue (**Table S2**). Because the N-terminal methionine was not detectable by MALDI-TOF MS, AAA was employed to confirm the overall AHA incorporation of 90.0% (**Table S2**).

Table 1. Percent composition of protein secondary structure predicted by CONTIN/LL software for circular dichroism data (CD) and through peak deconvolution of ATR-FTIR data pre- and post-Dox binding and chemical crosslinking via BS^3. CD data is reported as the average of three independent trials and ATR-FTIR data is reported as the average of two independent trials.

		% composition via CD			% composition via ATR-FTIR			
		α-helix	β-content	unordered	α-helix 1647-1660 cm^{-1}	β-content 1610-1640, 1675-1695 cm^{-1}	unordered (random coil) 1640-1647 cm^{-1}	other 1600-1610, 1660-1675 cm^{-1}
pH 4	Q_{WT}	56	21	23	66	22	4	8
	Q_{AHA}	55	24	21	63	31	-	6
+ Dox	Q_{WT}	36	22	43	55	34	1	10
	Q_{AHA}	22	32	46	47	34	8	11
+ Dox + BS^3	Q_{WT}	81	16	3	74	24	-	2
	Q_{AHA}	73	15	13	75	19	-	6

Secondary Structure of Q Proteins. To determine whether the incorporation of AHA impacted the secondary structure and thermostability of Q, CD spectroscopy was performed on Q_{WT} and Q_{AHA}. Both proteins exhibited similar secondary structure in 50 mM PB (**Figures S2, S3a**) with 56% and 55% α-helical content at pH 4.0 and 25°C for Q_{WT} and Q_{AHA}, respectively,

based on CONTIN/LL software [45-47] (**Table 1**, **S3**). This finding suggested that the incorporation of AHA maintained the overall secondary structure of Q. In addition, attenuated total reflectance-Fourier transform infrared (ATR-FTIR) spectroscopy was employed to better assess secondary structure in the solid state in anticipation of nano- to mesofiber assembly [30] (**Table 1, Figure S3**). ATR-FTIR of Q_{WT} and Q_{AHA} at pH 4.0 revealed significant peaks between 1647-1660 cm^{-1}, corresponding to the classical amide I band position for α-helical and multimeric coiled-coil proteins [48, 64, 65] (**Figure S3b-c**). Deconvolution of the IR spectra estimated 66% α-helicity for Q_{WT} and 63% for Q_{AHA} (**Table 1**), consistent with previously reported ATR-FTIR measurements of Q_{WT} [30].

Impact of Doxorubicin Binding on Secondary Structure. Based on previous studies of Q and its parent protein COMPcc [30, 31, 66, 67], along with modeling of Q•Dox docking (**Figure 1b**), we hypothesized that Q_{WT} and Q_{AHA} could encapsulate Dox and deliver the chemotherapeutic agent. First, we have confirmed the impact of binding to Dox prior the chemical crosslinking and the necessity of our design order by performing fluorescence spectroscopy at increasing ratios of Q:Dox and using One Site – Total and nonspecific binding kinetics in Prism to determine saturation. Binding of Dox prior to crosslinking appears to saturate at 2:1 ratio of Q:Dox. Binding kinetics analysis reveals a saturation point of ~5:1 ratio of Q:Dox indicating that one Dox molecule binds to five monomers of Q, which supports *in silico* docking results showing the ability for a Dox molecule to bind in the hydrophobic pocket of a Q pentamer (**Figure S4**). Similarly, binding of Dox to Q after chemical crosslinking and clicking of CMms6, the saturation point occurs at ~ also at 5:1 ratio of Q_{AHA}-X-CMms6:Dox by binding kinetics analysis indicating no significant difference in the encapsulation of Dox (**Figure S4**).

To assess if Dox binding affected the secondary structure of Q_{WT} and Q_{AHA}, CD and ATR-FTIR spectroscopy were conducted following overnight drug binding at room temperature (**Figure S3d-f**). Both CD and ATR-FTIR revealed that Dox binding reduced the α-helicity of Q_{WT}•Dox and Q_{AHA}•Dox (**Table 1, Figure S3d-f**). CD data revealed a reduction in the predicted α-helicity to 36% for Q_{WT}•Dox and 22% for Q_{AHA}•Dox (**Table 1, Figure S3d, Table S4**). Similarly, ATR-FTIR predicted a reduction in α-helicity, albeit less severe, with a 55% α-helical content for Q_{WT}•Dox and 47% for Q_{AHA}•Dox (**Table 1, Figure S3e-f**).

To stabilize the protein assembly following Dox binding, chemical crosslinking was performed using BS^3. Crosslinking was confirmed with 12% SDS-PAGE (**Figure S5**), demonstrating oligomeric protein bands with molecular weights greater than the 6.3 kDa monomeric Q, corresponding to covalently-associated dimer, trimer, tetramer, and pentamer populations [68]. Notably, crosslinking increased the α-helicity of Q_{WT}•Dox and Q_{AHA}•Dox as measured by CD and ATR-FTIR (**Table 1, Figure S3g-i, Table S4**). CD-derived α-helical content was 81% and 73% for crosslinked Q_{WT}•Dox (Q_{WT}•Dox_x) and Q_{AHA}•Dox (Q_{AHA}•Dox_x), respectively, with ATR-FTIR demonstrating 74% and 75%, respectively (**Table 1, Table S4**).

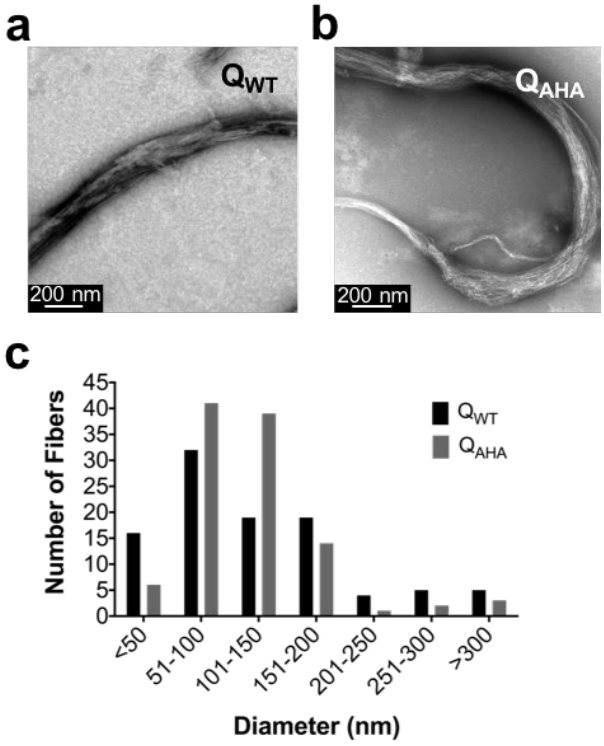

Figure 3. Transmission electron micrographs of (a) Q_{WT} and (b) Q_{AHA} at pH 4.0, negatively stained with 1% uranyl acetate. (c) Size distribution curve of nanofiber diameters observed via TEM.

Fiber Assembly. To assess whether the incorporation of AHA impacted fiber assembly, bright-field TEM of Q_{AHA} was conducted and compared to that of Q_{WT} [30]. Q_{WT} assembled into nanofibers bearing diameters of 126.6 ± 75.6 nm in diameter (18.6-359.1 nm, *N*=99) (**Figure 3a**), consistent with the size range previously observed for Q_{WT} [30], while Q_{AHA} exhibited nanofibers averaging 114.1 ± 57.5 nm (16.9-373.8 nm, *N*=107) (**Figure 3b**). Based on an unpaired two-tailed student's *t*-test, there was no statistically significant difference between Q_{WT} and Q_{AHA} fiber diameters (p = 0.31) (**Figure 3c**). Closer inspection of both sets of nanofibers revealed that they were composed of protofibrils. Q_{WT} protofibrils were 3.7 ± 0.4 nm in diameter (2.7-4.9 nm, *N*=115), while Q_{AHA} protofibrils were 3.7 ± 0.3 nm in diameter (2.9-4.3 nm, *N*=120), with no

significant size difference via unpaired two-tailed student's *t*-test (p = 0.42) (**Figure S9**). Protofibril sizes were comparable to the 3.5-3.6 nm protofibrils previously described, the diameters of which correspond to pentameric helical bundles [30, 67].

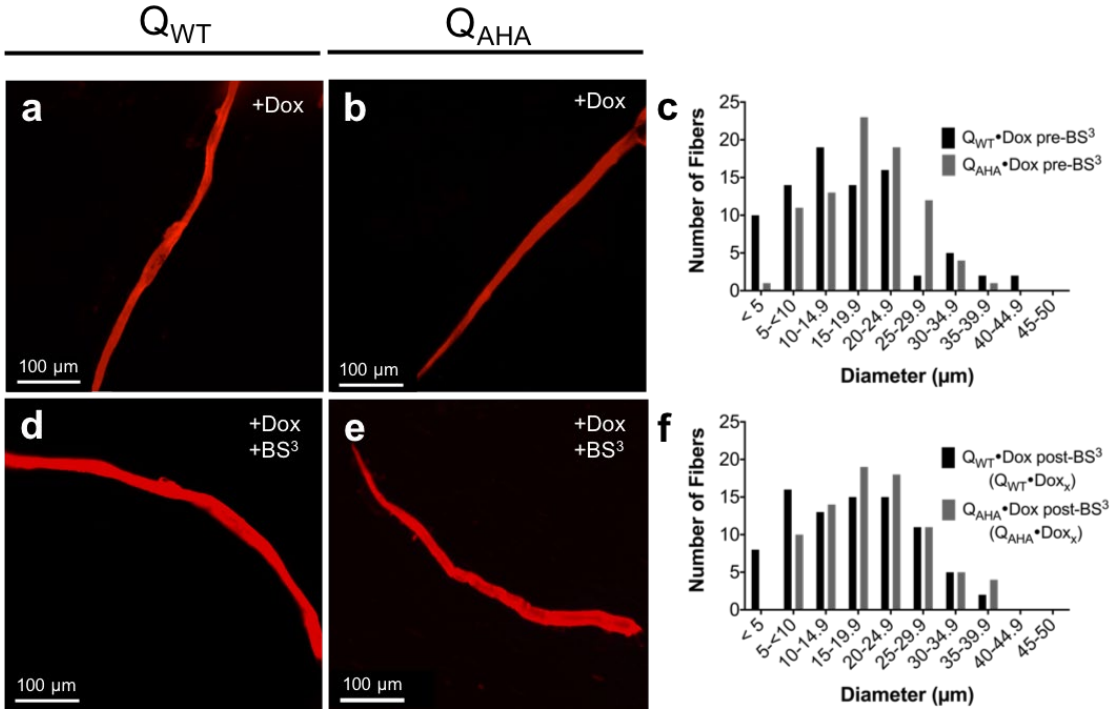

Figure 4. Fluorescence microscopy of Dox-bound (a) Q_{WT} and (b) Q_{AHA} and (c) their size distributions pre-BS^3 crosslinking. Fluorescence microscopy of Dox-bound and BS^3-crosslinked (d) Q_{WT} and (e) Q_{AHA} and (f) their size distributions.

Previous studies demonstrated that further fiber assembly, from the nanoscale to the mesoscale, resulted from curcumin binding by Q [30, 67]. Due to the ability for Q protein fibers to bind curcumin [30], fiber assembly was also assessed here in the presence of Dox. Firstly, in the presence of only the co-solvent used to dissolve Dox, 1% dimethyl sulfoxide (DMSO), protein nanofibers were maintained, as visualized on TEM, without evident mesofiber assembly (**Figure**

S6). However, mesoscale fiber assembly was visualized *via* fluorescence microscopy following overnight Dox binding (**Figure 4a-c**) with average diameters of 16.2 ± 9.4 μm (2.5-42.3 μm, *N*=84) for Q_{WT}•Dox (**Figure 4a,c**) and 18.6 ± 7.2 μm (3.6-36.1 μm, *N*=84) for Q_{AHA}•Dox (**Figure 4b,c**). Chemical crosslinking *via* BS^3 yielded Dox-bound proteins (**Figure 4d-f**) with similar diameters of 16.9 ± 8.9 μm (3.5-38.3 μm, *N*=85) for Q_{WT}•Dox_x (**Figure 4d, f**) and 19.7 ± 7.9 μm (5.7-38.1 μm, *N*=81) for Q_{AHA}•Dox_x (**Figure 4e, f**), maintaining the fiber diameters of the non-crosslinked fibers. While the incorporation of AHA did not disrupt mesofiber assembly, a two-way ANOVA statistical test between Q_{WT}•Dox and Q_{AHA}•Dox pre- and post-BS^3 crosslinking determined that Q_{AHA}•Dox resulted in thicker fibers than Q_{WT}•Dox both pre- and post-crosslinking (**, $p = 0.0045$). By contrast, the crosslinking status had no effect on fiber diameter ($p = 0.31$).

CMms6 Conjugation *via* Azide-alkyne Cycloaddition. Conjugation of crosslinked Q_{AHA} mesofibers to iron oxide-templating CMms6 was investigated to generate a USPIO-bearing MRI-traceable agent. Room temperature copper-catalyzed azide-alkyne cycloaddition click chemistry [69] was performed between the alkyne-functionalized CMms6 and azide-bearing Q_{AHA}•Dox_x fibers, with Q_{WT}•Dox_x fibers as a negative control. Reaction of Q_{AHA}•Dox_x with CMms6 was confirmed by MALDI-TOF (**Figure S7**). SDS-PAGE analysis of Q_{AHA}•Dox_x showed positive shifts in the molecular weight of its oligomeric bands (**Figure S8**, solid boxes) by approximately 3 kDa, the molecular weight of CMms6, in the presence of the peptide (**Figure S8**, dashed box).. These bands were maintained following dialysis to remove excess peptide, demonstrating successful conjugation between crosslinked Q_{AHA} and CMms6, resulting in the product Q_{AHA}-X-

CMms6. The negative control, Q_{WT}•Dox_x fibers, showed no change in molecular weight in the presence of CMms6 due to the absence of the azide moiety necessary for conjugation (**Figure S8**).

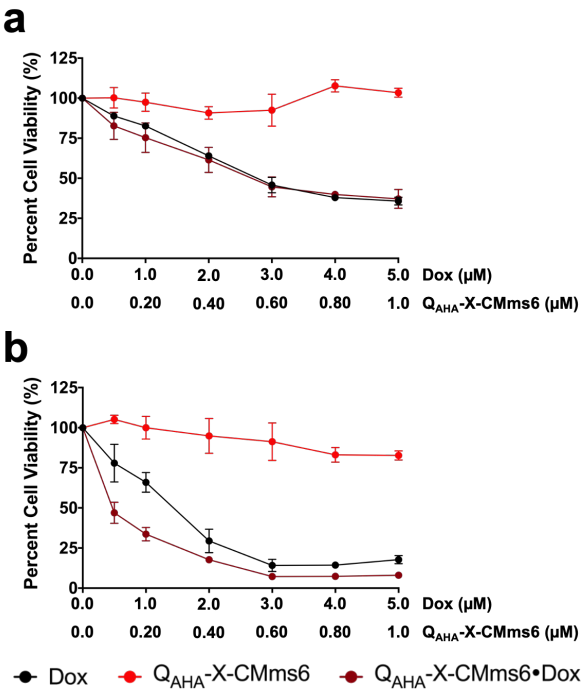

Figure 5. Percent viability of the MCF-7 cell line *via* CCK8-assay following (a) 24 hr and (b) 48 hr treatment with Dox alone, crosslinked Q_{AHA}-X-CMms6 alone, or Dox-bound Q_{AHA}-X-CMms6●Dox where the ratio of Q_{AHA}-X-CMms6:Dox is maintained at 1:5 per fluorescence spectroscopy-based binding studies. All plots depict the average of three independent trials and their standard deviations following baseline subtraction and normalization to cells treated with buffer (50 mM PB, pH 7.4 + 0.1% DMSO).

Therapeutic Efficacy of Drug-loaded Protein. With the successful encapsulation of Dox and CMms6-conjugated fiber assembly, the therapeutic efficacy of Q_{AHA}-X-CMms6 was compared to that of Dox alone on the Dox-sensitive MCF-7 human breast adenocarcinoma cell line. Iron oxide particles have notoriously interfered with *in vitro* cell viability assays, in the presence of both

absorbance and fluorescence-based probes [70]. Therefore, the therapeutic efficacy of the agent was studied *in vitro* prior to iron oxide templation. Cells were treated with either Dox alone, Q_{AHA}-X-CMms6, or Q_{AHA}-X-CMms6•Dox. After treatment for 24 hr or 48 hr, a CCK8 cell viability assay was conducted and the IC_{50} values were calculated (**Figure 5**, **Table S5**). Q_{AHA}-X-CMms6 alone had no significant effect on cell viability after 24 hr or 48 hr treatment; therefore, IC_{50} values for Q_{AHA}-X-CMms6 could not be determined (**Figure 5**). By contrast, after 24 hr treatment, Dox and Q_{AHA}-X-CMms6•Dox both reduced cell viability with increasing Dox concentrations (**Figure 5a**), resulting in IC_{50} values of 2.92 ± 0.23 μM (N=3) and 2.74 ± 0.31 μM (N=3), respectively (**Table S5)**. Following 48 hr treatment, Dox and Q_{AHA}-X-CMms6•Dox further decreased cell viability (**Figure 5b**), resulting in reduced IC_{50} values of 1.28 ± 0.22 μM (N=3) for Dox alone and 0.48 ± 0.11 μM (N=3) for Q_{AHA}-X-CMms6•Dox (**Table S5)**. Tukey's HSD test for multiple pair-wise comparisons was used to test for significance between the treatments and the treatment periods studied. After 24 hr treatment, there was no significant difference between the IC_{50} values of Dox and Q_{AHA}-X-CMms6•Dox (p = 0.78), suggesting that Dox delivery by Q_{AHA}-X-CMms6 did not significantly improve the effect of Dox on MCF-7 cells at this time point. After 48 hr treatment, the IC_{50} of Dox decreased significantly (***, p = 0.0001) as did the IC_{50} of Q_{AHA}-X-CMms6•Dox (****, $p < 0.0001$). Notably, the IC_{50} value of Q_{AHA}-X-CMms6•Dox at 48 hr was appreciably lower than that of Dox at 48 hr (*, p = 0.01), suggesting that binding and release by Q_{AHA}-X-CMms6 improved the therapeutic effect of Dox on the MCF-7 cell line following 48 hr treatment. This also suggests that the mesofibers provide a more concentrated and sustained release of doxorubicin overtime for a cumulative potency to the cells.

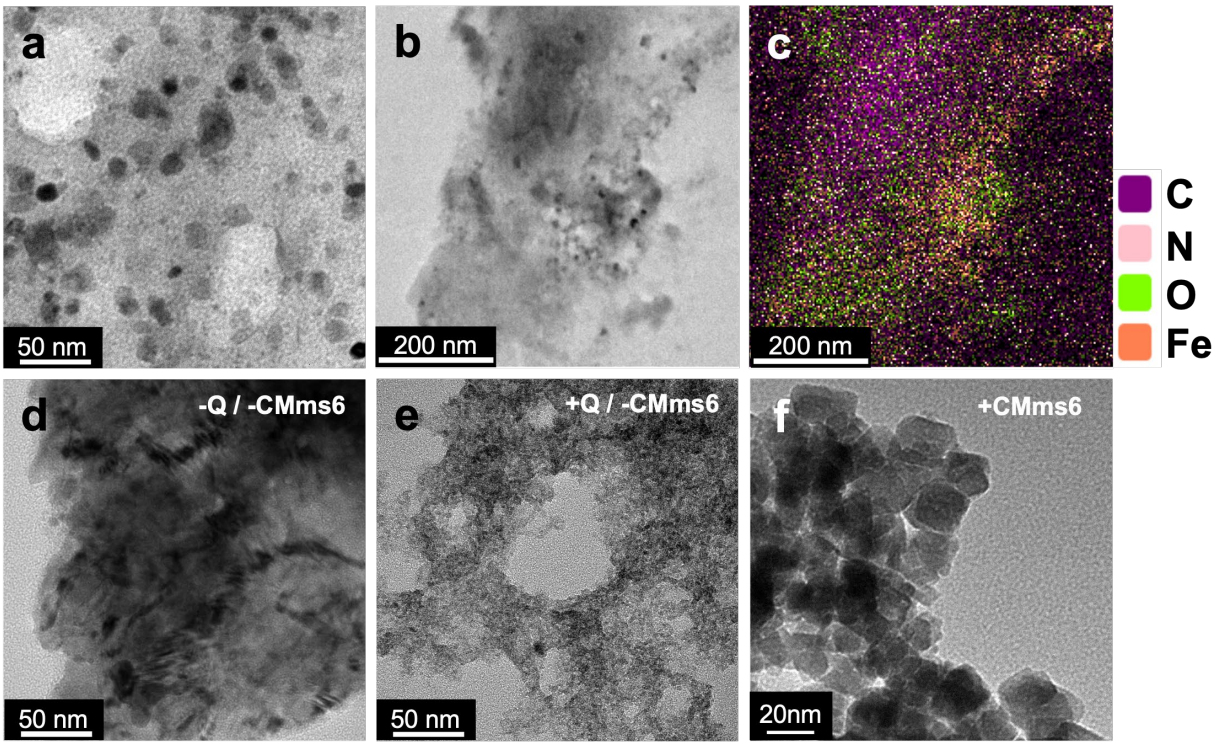

Figure 6. Characterization of USPIOs synthesized *via* co-precipitation reaction in the absence of protein staining and presence of Q_{AHA}-X-CMms6 *via* (a) high-resolution TEM and (b) low-resolution TEM of Q_{AHA}-X-CMms6•USPIO assessed *via* elemental mapping by (c) energy dispersive X-ray spectroscopy. High-resolution TEM in (d) the absence of both Q and CMms6, (e) in the presence of Q_{AHA} alone, and (f) in the presence of CMms6 alone.

Iron Oxide Nanoparticle Synthesis and Characterization. Iron co-precipitation was performed to assess whether the protein-peptide conjugate could template USPIOs. Room temperature USPIO co-precipitation was carried out in the presence and absence of CMms6, Q_{AHA}-X-CMms6, and crosslinked mesoscale Q_{AHA} (Q_{AHA}•Dox_x) serving as a negative control. An unorganized aggregation of iron oxide was observed on TEM following precipitation in the absence of both Q_{AHA} and CMms6 (**Figure 6d**). Q_{AHA}, in the absence of CMms6, resulted in unorganized iron oxide and small heterogeneously shaped particles (**Figure 6e**). By contrast,

CMms6 alone organized highly crystalline cuboidal USPIOs (**Figure 6f**) with average diameters of 17.4 ± 3.6 nm (9.9-29.3 nm, *N*=152) (**Figure S9**), consistent with USPIOs previously synthesized by a similar CMms6 peptide [22]. The Q_{AHA}-X-CMms6 conjugate also produced cuboidal USPIOs with average diameters of 14.1 ± 3.1 nm (6.3-25.5 nm, *N*=151) overlaid onto fibrous protein networks, resulting in the Q_{AHA}-X-CMms6•USPIO hybrid material (**Figure 6a**).

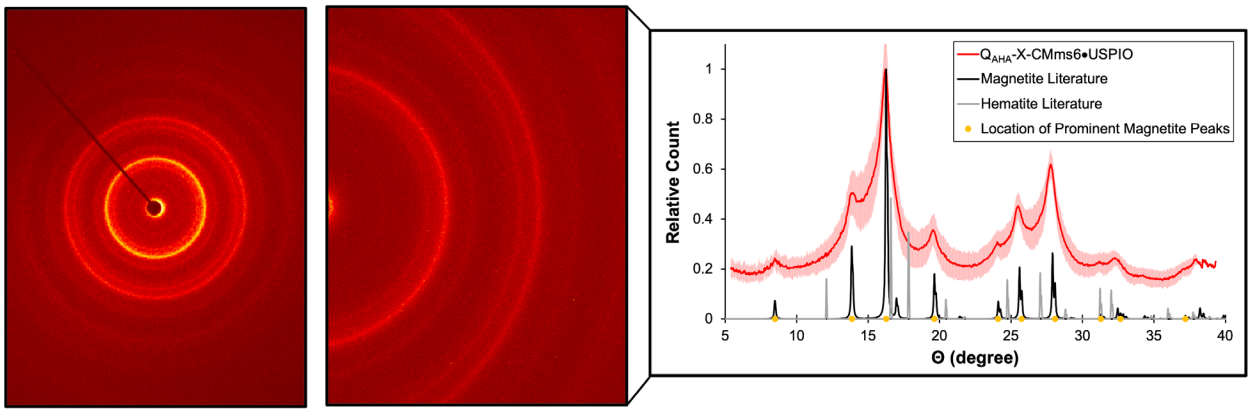

Figure 7. X-RAY Diffraction pattern of Q_{AHA}-X-CMms6•USPIO demonstrating distinct concentric rings correlating to the lattice *d*-spacing of the particles. The XRD angle peaks of Q_{AHA}-X-CMms6•USPIO (red) are compared to those of magnetite (black) and hematite (gray) and reported as the mean value ± standard deviation.

Small angle electron diffraction (SAED) mode and energy dispersive X-ray spectroscopy (EDS) were employed to confirm that the particles synthesized were, in fact, magnetite-based USPIOs and that they were co-localized with the protein-peptide conjugate by which they were templated. As expected, Q_{AHA}-X-CMms6-templated USPIOs, Q_{AHA}-X-CMms6•USPIO, demonstrated distinct concentric rings typically seen in polycrystalline samples composed of randomly oriented crystallites [71] (**Figure 7**). Q_{AHA}-X-CMms6•USPIO showed a near exact match to the diffraction

angles of the reference crystal structure of magnetite produced by *Bragg et al* (**Figure 7**) [72, 73]. The byproduct from incomplete coprecipitation is hematite which gives a distinctly different pattern; also compared in **Figure 7** [74]. The *d*-spacing values for these USPIOs were also calculated (**Table S6**) and compared to those of magnetite (Fe_3O_4). The calculated *d*-spacing values for nanoparticles synthesized by Q_{AHA}-X-CMms6 were in agreement with previously described values for magnetite/maghemite [72-74] confirming that magnetite and/or maghemite-based USPIOs had been generated.

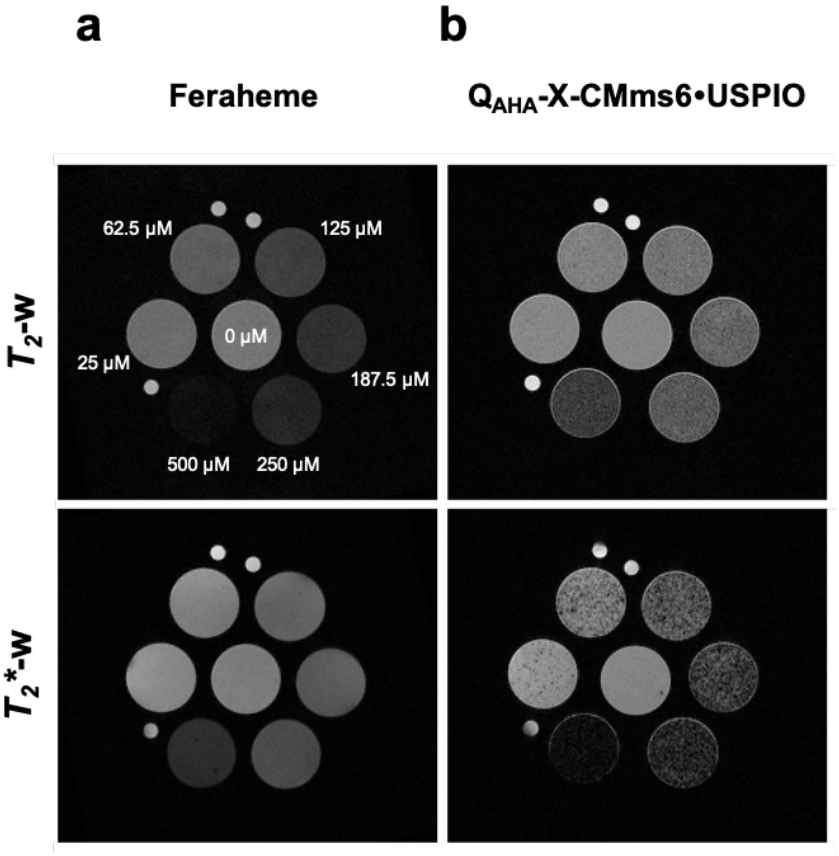

Figure 8. T_2 and T_2*-weighted MRI at 7-T comparing the induced contrast between (a) Feraheme and (b) Q_{AHA}-X-CMms6•USPIO in 1% agarose phantom samples.

Table 2. Relaxivity values from magnetic resonance relaxation of Feraheme and Q_{AHA}-X-CMms6•USPIO. Data is reported as the mean value ± standard deviation of three independent trials.

Sample	r_1 (mM^{-1} s^{-1})	r_2 (mM^{-1} s^{-1})	r_2* (mM^{-1} s^{-1})	r_2/r_1	r_2*/r_2
Feraheme	1.63 ± 0.15	87.03 ± 4.74	93.04 ± 6.76	53.66 ± 4.87	1.07 ± 0.04
Q_{AHA}-X-CMms6•USPIO	0.17 ± 0.01	19.76 ± 5.60	316.88 ± 39.79	116.23 ± 33.64	16.03 ± 0.31

Phantom Magnetic Resonance Imaging. T_1 , T_2 and T_2* MR relaxation time studies were conducted at 7-T to assess the diagnostic potential for this protein-USPIO hybrid biomaterial in comparison to the FDA-approved, USPIO-based Feraheme. While T_1 mapping showed minimal brightening effect for Feraheme and Q_{AHA}-X-CMms6•USPIO (**Figure S11 and Figure S12**), the effect was significantly lower for the hybrid biomaterial (****, $p < 0.0001$), with a longitudinal relativity (r_1) value of 0.17 ± 0.01 $mM^{-1}s^{-1}$, compared to 1.63 ± 0.15 $mM^{-1}s^{-1}$ for Feraheme, based on an unpaired student's *t*-test (**Table 2**). The corresponding relaxation rates, R_2 and R_2*, demonstrated linear relationships with the concentration of iron in the phantom samples of both Feraheme and Q_{AHA}-X-CMms6•USPIO. Feraheme showed a stronger darkening effect than Q_{AHA}-X-CMms6•USPIO using a T_2-weighted sequence (**Figure 8**) resulting in a transverse relaxivity (r_2) value of 87.03 ± 4.74 $mM^{-1}s^{-1}$ for Feraheme compared to 19.76 ± 5.60 $mM^{-1}s^{-1}$ for Q_{AHA}-X-CMms6•USPIO and (**Table 2**). However, the hybrid biomaterial demonstrated superior T_2* effect over Feraheme (**Figure 8**) with a relaxivity r_2* of 316.88 ± 39.79 $mM^{-1}s^{-1}$ for Q_{AHA}-X-CMms6•USPIO that was 3.41-fold higher than that of Feraheme at 93.04 ± 6.76 $mM^{-1}s^{-1}$ (**Table**

2). Comparing the r_2 and r_2* values of Feraheme and Q_{AHA}-X-CMms6•USPIO, *via* Tukey's HSD test for multiple pair-wise comparisons, the r_2 of Feraheme was significantly higher than that of Q_{AHA}-X-CMms6•USPIO (***, $p = 0.0001$), while the the r_2* of Q_{AHA}-X-CMms6•USPIO was significantly higher than that of Feraheme (****, $p < 0.0001$), (**Table 2, Figure S11**). The r_2 and r_2* values of Feraheme showed no significant difference ($p = 0.77$), while the r_2* of Q_{AHA}-X-CMms6•USPIO was significantly higher than its r_2 (****, $p < 0.0001$) (**Table 2**). A comparison of r_2*/r_2 ratios is also suggestive of contrast agent effectiveness for T_2*-weighted imaging [75]. The r_2*/r_2 value of Q_{AHA}-X-CMms6•USPIO was 15-fold higher than that of Feraheme (**Table 2**), showing a highly sensitive T_2* effect by the hybrid construct compared to Feraheme at 7-T.

***In vivo* Magnetic Resonance Imaging:**

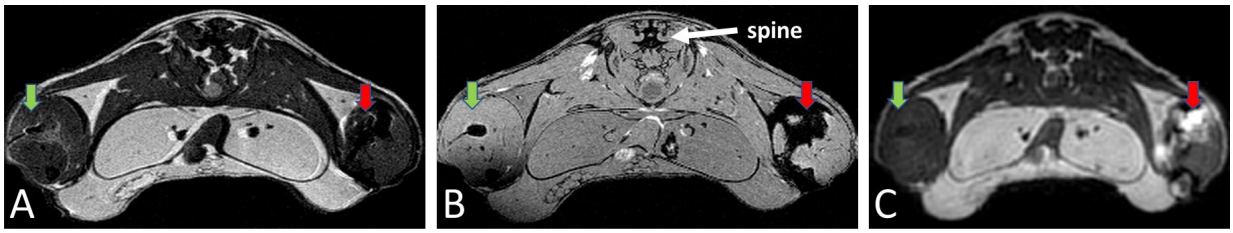

Figure 9. *In vivo* MRI of a C57Bl6 mouse acquired at 7-T using (a) T_2 and (b) T_2*-weighted and (c) T_1-weighted imaging to illustrate the induced contrast by Q_{AHA}-X-CMms6•USPIO injected in the left hindlimb (depicted by the green arrow) and Feraheme injected in the right hindlimb (red arrow). While both nano-agents induce effective T_2/T_2*-weighted darkening in (a) and (b) only Feraheme results in T_1-brightening using ultrashort echo time imaging suggesting the lack of water coordination QAHA-X-CMms6•USPIO.

DISCUSSION

We present a protein-iron oxide hybrid biomaterial for use as a diagnostic agent by combining a drug-encapsulating rationally-designed protein with MRI-detectable USPIOs *via* conjugation to a biomimetic peptide for iron oxide synthesis. Hybrid organic-inorganic materials have become increasingly of interest in diagnostic development, but studies thus far have largely utilized proteins with non-specific drug binding capabilities [76, 77] and USPIOs synthesized under harsh non-polar conditions [16, 17, 78]. While biomimetic proteins and peptides have been explored for USPIO synthesis [21-23, 79], the utilization of milder nanoparticle synthesis techniques is lacking in the development of these agents. In contrast to previous work, here we capitalize on NCAA incorporation [26, 27] and bioorthogonal conjugation [26], specifically azide-alkyne cycloaddition [28], to synthesize a protein-peptide conjugate capable of encapsulating Dox and of serving as a template for biomimetic USPIO synthesis. As a result, a protein-iron oxide hybrid has been synthesized under aqueous conditions.

Residue-specific AHA incorporation further functionalizes the Q protein [30] for biorthogonal conjugation, while maintaining a nanofiber self-assembly that is consistent with Q_{WT} (**Table 1, Figures 2, S2, S3, Tables S3, S4**). The negligible differences in secondary structure contributed by AHA were expected given the molecular weight difference of only 5 Da between AHA and methionine. Additionally, both Q_{WT} and Q_{AHA} are capable of binding to chemotherapeutic Dox, which results in further fiber assembly to generate mesoscale drug-bound fibers (**Figure 4**), similar to previously reported results for curcumin-bound Q_{WT} protein[30]. In

contrast to Q_{WT}, Q_{AHA} demonstrates successful bioorthogonal conjugation to the alkyne-bearing CMms6 peptide *via* azide-alkyne cycloaddition (**Figure S7, S8**).

We also investigate whether the bioorthogonal conjugation impacts the ability of CMms6 to organize USPIOs. While magnetosome-associated Mms6 and its C-terminus CMms6 have previously demonstrated USPIO biomineralization outside of magnetotactic bacteria [20, 22], their capacity for controlled USPIO synthesis has not been explored following chemical conjugation to proteins of interest. However, TEM analysis reveals that both the propargylglycine-bearing CMms6 alone and Q_{AHA}-X-CMms6 are able to synthesize distinct magnetite-based USPIOs (**Figures 6a, S10, Table S6)**. XRD patterns of Q_{AHA}-X-CMms6•USPIO show concentric rings typical of a magnetite polycrystalline sample [72] (**Figure 7**), in agreement with the observed cluster of closely arranged USPIOs.

The small size of USPIOs can serve dual purposes by producing both high longitudinal R_1- and transverse R_2- and R_{2*}-relaxivities when optimized coatings combined with favorable experimental imaging conditions are achieved (low doses, magnetic field strength ≤3-Tesla and imaging sequences enabling sub-millisecond echo times) resulting in either brightening or darkening signal contrast enhancement [59]. However, the needs to perform imaging at ultrahigh magnetic field (strength ≥7 Tesla) in order to gain sensitivity or achieve high anatomical details, especially in preclinical imaging makes most USPIO agents primarily used as T_2/T_2* contrast agents [10, 61-63]. MR imaging and relaxation studies validate that this protein-iron oxide hybrid agent provides shortened T_2/T_2*-relaxation times, with a significantly more dramatic shortening of T_2* in comparison to the FDA-approved standard USPIO agent, Feraheme. Feraheme is, however, a more sensitive T_2 agent compared to Q_{AHA}-X-CMms6•USPIO (**Figures 8a-b, S10 and Table 2**). The lower r_2 for Q_{AHA}-X-CMms6•USPIO compared to Feraheme is likely due to the larger

hydrodynamic size of the fiber [80, 81]. Notably, the sequestering of USPIOs within the protein-peptide conjugate prevents the protons of surrounding water molecules from closely interacting with the magnetic core of the USPIOs resulting in low transverse relaxivity r_2 [82]. This is also reflected by the lack of the QAHA-X-CMms6•USPIO T_1-brigthening shown in the *in vivo* experiments.

However, combining a multitude of USPIOs spaced along a single protein fiber increases the overall USPIO distribution area within the hybrid material, amplifying the agent's effect on field heterogeneity and resulting in a highly sensitive T_2* effect consistent with the static dephasing regime theory [83-85] (**Figures 8a-b, S8, Table 2**). As a result, Q_{AHA}-X-CMms6•USPIO provides a 3.41-fold higher r_2* than Feraheme. The high r_2*/r_2 ratio of Q_{AHA}-X-CMms6•USPIO indicates that the agent could indeed act as a highly sensitive T_2* agent (**Table 2**). Furthermore, *in vivo* imaging of Q_{AHA}-X-CMms6 (**Figure 9**) confirms its contrast darkening effectiveness in muscle tissue using both T_2/T_2*-weighting. The hypointense contrast effect induced by the presence of both IO nano-agents appears to be more confined with the Q_{AHA}-X-CMms6 biomaterial due to its self-assembling nature (green arrow). On the other hand, Feraheme is more spread-out throughout the gastrocnemius muscle due to its smaller size (red arrow) resulting in a larger darkening area. The large area spread within the muscle is confirmed with Feraheme's T_1-signal brightening in the left hindlimb muscle using the ultrashort echo time imaging sequence (c, red arrow) while the lack of signal from the Q biomaterial illustrates the likely lack of water coordination with the IO incorporated in the fiber.

The successful conjugation of a multitude of USPIOs to a single protein fiber enabled to achieve a higher iron payload per construct. This can be particularly effective at amplifying magnetic field distortions resulting in the strong T_2* effect demonstrated by Q_{AHA}-X-

CMms6•USPIO [86],[87].

CONCLUSIONS

We have used rational design in protein engineering coupled with bioorthogonal conjugation chemistry to create a protein-iron oxide hybrid biomaterial synthesized under mild, aqueous conditions. The Q_{AHA}-X-CMms6 protein demonstrates the encapsulation of Dox within the protein mesofibers without the need for covalent conjugation to the chemotherapeutic agent. Dox encapsulation and BS^3 crosslinking stabilize the protein's structure, further enhancing its drug delivery potential. Because the protein fibers are biosynthesized *via* residue-specific NCAA incorporation of an azide-functionalized residue, subsequent bioorthogonal conjugation to an alkyne-functionalized iron oxide templating peptide allows for the organization of USPIOs under aqueous conditions. Linking the protein to MRI-detectable USPIOs greatly improves the ability to localize and track the protein fiber with much higher r_2* molar relaxivity at 7-T compared to Feraheme. The high T_2*-weighted MRI sensitivity suggests that the characterized construct holds promise as a protein-based biomaterail with traceable or diagnostic capabilities, with potential to encapsulate and deliver a range of small molecule therapeutics.

ASSOCIATED CONTENT

Electronic Supplementary Information is available.

AUTHOR INFORMATION

Corresponding Author

*Email: Montclare@nyu.edu

ORCID

Lindsay K. Hill: 0000-0002-1833-8574

Dustin Britton: 0000-0001-6943-3064

Teeba Jihad: 0000-0003-1489-2479

Xuan Xie: 0000-0003-2295-6751

Erika Delgado-Fukushima: 0000-0003-4030-1345

Che Fu Liu: 0000-0001-6280-3245

Orin Mishkit : 0000-0002-0858-5053

Chengliang Liu: 0000-0002-7322-8589

Chunhua Hu : 0000-0002-8172-2202

Michael Meleties: 0000-0003-1621-9835

P. Douglas Renfrew: 0000-0003-4267-2932

Richard Bonneau: 0000-0003-4354-7906

Youssef Z. Wadghiri: 0000-0001-7175-9397

Jin Kim Montclare: 0000-0001-6857-3591

Author Contributions

The manuscript was written through contributions of all authors. All authors have given approval to the final version of the manuscript.

Funding Sources

This work was supported by NSF-MRSEC Program under Award Number DMR 1420073 and NSF-DMREF under Award Number DMR 1728858, as well as the Shifrin-Myers Breast Cancer Discovery Fund. Part of this work was performed at the NYU Langone Health Preclinical Imaging Laboratory, a shared resource partially supported by the NIH/SIG 1S10OD018337-01, the Laura and Isaac Perlmutter Cancer Center Support Grant, NIH/NCI 5P30CA016087, and the NIBIB Biomedical Technology Resource Center Grant NIH P41 EB017183. This research also used resources of the Center for Functional Nanomaterials, which is a U.S. DOE Office of Science Facility, at the Brookhaven National Laboratory under Contract No. DE-SC0012704 for TEM measurements. MALDI-TOF MS and ATR-FTIR experiments were performed at the NYU Chemistry Department Shared Instrument Facility. The research used the X-ray Diffraction Facility of Department of Chemistry at New York University which is supported by the National Science Foundation (NSF) Chemistry Research Instrumentation and Facilities Program (CHE-0840277) and Materials Research Science and Engineering Center (MRSEC) Program (DMR-1420073).

The authors declare no competing financial interests.

ACKNOWLEDGEMENTS

The authors thank C. Lin and R. McLurkin of the NYU Chemistry Department Shared Instrument Facility for training on MALDI-TOF and ATR-FTIR. The authors also thank Dr. César Berríos-Otero for his assistance in MRI phantom preparation and data processing. The facility is supported by the National Science Foundation (NSF) Chemistry Research Instrumentation and Facilities Program (CHE-0840277) and Materials Research Science and Engineering Center (MRSEC) Program (DMR-1420073).

For Table of Contents Only

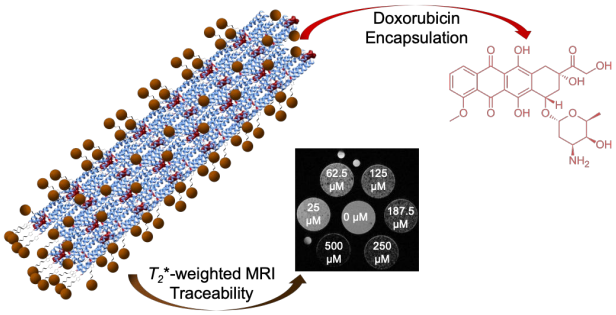

REFERENCES

1. Kelkar, S.S. and T.M. Reineke, *Theranostics: Combining Imaging and Therapy.* Bioconjugate Chemistry, 2011. **22**(10): p. 1879-1903.
2. Howard, D., et al., *Tissue engineering: strategies, stem cells and scaffolds.* Journal of anatomy, 2008. **213**(1): p. 66-72.
3. Yin, L., C. Yuvienco, and J.K. Montclare, *Protein based therapeutic delivery agents: Contemporary developments and challenges.* Biomaterials, 2017. **134**: p. 91-116.
4. Nam, S.Y., et al., *Imaging strategies for tissue engineering applications.* Tissue Eng Part B Rev, 2015. **21**(1): p. 88-102.
5. Kharbikar, B.N., et al., *Theranostic biomaterials for tissue engineering.* Current Opinion in Biomedical Engineering, 2021. **19**: p. 100299.
6. Clavijo Jordan, V., M.R. Caplan, and K.M. Bennett, *Simplified synthesis and relaxometry of magnetoferritin for magnetic resonance imaging.* Magnetic Resonance in Medicine, 2010. **64**(5): p. 1260-1266.
7. Janke, H.P., et al., *Labeling of Collagen Type I Templates with a Naturally Derived Contrast Agent for Noninvasive MR Imaging in Soft Tissue Engineering.* Advanced Healthcare Materials, 2018. **7**(18): p. 1800605.
8. Hu, S., et al., *Enhanced bone regeneration and visual monitoring via superparamagnetic iron oxide nanoparticle scaffold in rats.* J Tissue Eng Regen Med, 2018. **12**(4): p. e2085-e2098.
9. Mastrogiacomo, S., et al., *A theranostic dental pulp capping agent with improved MRI and CT contrast and biological properties.* Acta Biomater, 2017. **62**: p. 340-351.
10. Mao, X., J. Xu, and H. Cui, *Functional nanoparticles for magnetic resonance imaging.* Wiley Interdiscip Rev Nanomed Nanobiotechnol, 2016. **8**(6): p. 814-841.
11. Kumar, C.S. and F. Mohammad, *Magnetic nanomaterials for hyperthermia-based therapy and controlled drug delivery.* Adv Drug Deliv Rev, 2011. **63**(9): p. 789-808.
12. Daldrup-Link, H.E., et al., *MRI of tumor-associated macrophages with clinically applicable iron oxide nanoparticles.* Clin Cancer Res, 2011. **17**(17): p. 5695-704.
13. Wang, Y.X., *Superparamagnetic iron oxide based MRI contrast agents: Current status of clinical application.* Quant Imaging Med Surg, 2011. **1**(1): p. 35-40.
14. Khurana, A., et al., *Ferumoxytol: a new, clinically applicable label for stem-cell tracking in arthritic joints with MRI.* Nanomedicine (Lond), 2013. **8**(12): p. 1969-83.
15. Mok, H. and M. Zhang, *Superparamagnetic iron oxide nanoparticle-based delivery systems for biotherapeutics.* Expert Opin Drug Deliv, 2013. **10**(1): p. 73-87.
16. Quan, Q., et al., *HSA Coated Iron Oxide Nanoparticles as Drug Delivery Vehicles for Cancer Therapy.* Mol. Pharm., 2011. **8**: p. 1669–1676.
17. Semkina, A., et al., *Core-Shell-Corona Doxorubicin-Loaded Superparamagnetic Fe3O4 Nanoparticles for Cancer Theranostics.* Colloids Surf. B, Biointerfaces 2015. **136**: p. 1073–1080.
18. Abakumov, M.A., et al., *Visualization of Experimental Glioma C6 by MRI with Magnetic Nanoparticles Conjugated with Monoclonal Antibodies to Vascular Endothelial Growth Factor.* Bull Exp Biol Med, 2012. **154**: p. 274–277.

19. Crookes-Goodson, W.J., J.M. Slocik, and R.R. Naik, *Bio-directed synthesis and assembly of nanomaterials.* Chemical Society Reviews, 2008. **37**(11): p. 2403-2412.
20. Arakaki, A., J. Webb, and T. Matsunaga, *A novel protein tightly bound to bacterial magnetic particles in Magnetospirillum magneticum strain AMB-1.* J Biol Chem, 2003. **278**(10): p. 8745-50.
21. Amemiya, Y., et al., *Controlled formation of magnetite crystal by partial oxidation of ferrous hydroxide in the presence of recombinant magnetotactic bacterial protein Mms6.* Biomaterials, 2007. **28**(35): p. 5381-9.
22. Arakaki, A., et al., *Control of the morphology and size of magnetite particles with peptides mimicking the Mms6 protein from magnetotactic bacteria.* J Colloid Interface Sci, 2010. **343**(1): p. 65-70.
23. Prozorov, T., et al., *Protein-Mediated Synthesis of Uniform Superparamagnetic Magnetite Nanocrystals.* Advanced Functional Materials, 2007. **17**(6): p. 951-957.
24. Rawlings, A.E., et al., *Ferrous Iron Binding Key to Mms6 Magnetite Biomineralisation: A Mechanistic Study to Understand Magnetite Formation Using pH Titration and NMR Spectroscopy.* Chemistry, 2016. **22**(23): p. 7885-94.
25. Chica, R.A., *Protein engineering in the 21st century.* Protein science : a publication of the Protein Society, 2015. **24**(4): p. 431-433.
26. Lang, K. and J.W. Chin, *Cellular Incorporation of Unnatural Amino Acids and Bioorthogonal Labeling of Proteins.* Chemical Reviews, 2014. **114**(9): p. 4764-4806.
27. Voloshchuk, N. and J.K. Montclare, *Incorporation of unnatural amino acids for synthetic biology.* Mol Biosyst, 2010. **6**(1): p. 65-80.
28. Kolb, H.C., M.G. Finn, and K.B. Sharpless, *Click Chemistry: Diverse Chemical Function from a Few Good Reactions.* Angew Chem Int Ed Engl, 2001. **40**(11): p. 2004-2021.
29. Hein, J.E. and V.V. Fokin, *Copper-catalyzed azide–alkyne cycloaddition (CuAAC) and beyond: new reactivity of copper(i) acetylides.* Chemical Society Reviews, 2010. **39**(4): p. 1302-1315.
30. Hume, J., et al., *Engineered Coiled-Coil Protein Microfibers.* Biomacromolecules, 2014. **15**(10): p. 3503-3510.
31. Gunasekar, S.K., et al., *N-Terminal Aliphatic Residues Dictate the Structure, Stability, Assembly, and Small Molecule Binding of the Coiled-Coil Region of Cartilage Oligomeric Matrix Protein.* Biochemistry, 2009. **48**(36): p. 8559-8567.
32. Chou, S.F., D. Carson, and K.A. Woodrow, *Current strategies for sustaining drug release from electrospun nanofibers.* J Control Release, 2015. **220**(Pt B): p. 584-91.
33. Link, A.J. and D.A. Tirrell, *Cell surface labeling of Escherichia coli via copper(I)-catalyzed [3+2] cycloaddition.* J Am Chem Soc, 2003. **125**(37): p. 11164-5.
34. Link, A.J., M.K. Vink, and D.A. Tirrell, *Presentation and detection of azide functionality in bacterial cell surface proteins.* J Am Chem Soc, 2004. **126**(34): p. 10598-602.
35. Speth, P.A., Q.G. van Hoesel, and C. Haanen, *Clinical pharmacokinetics of doxorubicin.* Clin Pharmacokinet, 1988. **15**(1): p. 15-31.
36. Beijnen, J.H., O.A.G.J. van der Houwen, and W.J.M. Underberg, *Aspects of the degradation kinetics of doxorubicin in aqueous solution.* International Journal of Pharmaceutics, 1986. **32**(2): p. 123-131.

37. Wu, D.C. and C.M. Ofner, 3rd, *Adsorption and degradation of doxorubicin from aqueous solution in polypropylene containers.* AAPS PharmSciTech, 2013. **14**(1): p. 74-7.
38. Marek, S.R., et al., *Intelligent, responsive and theranostic hydrogel systems for controlled delivery of therapeutics.* RSC Smart Materials, 2015. **2015**: p. 10-43.
39. Kothiwale, S., J.L. Mendenhall, and J. Meiler, *BCL::Conf: small molecule conformational sampling using a knowledge based rotamer library.* Journal of Cheminformatics, 2015. **7**(1): p. 47.
40. DeLuca, S., K. Khar, and J. Meiler, *Fully Flexible Docking of Medium Sized Ligand Libraries with RosettaLigand.* PLoS One, 2015. **10**(7): p. e0132508.
41. Tanrikulu, I.C., et al., *Discovery of Escherichia coli methionyl-tRNA synthetase mutants for efficient labeling of proteins with azidonorleucine in vivo.* Proceedings of the National Academy of Sciences, 2009. **106**(36): p. 15285.
42. Wilkins, M.R., et al., *Detailed peptide characterization using PEPTIDEMASS--a World-Wide-Web-accessible tool.* Electrophoresis, 1997. **18**(3-4): p. 403-8.
43. Wilkins, M.R., et al., *Protein identification and analysis tools in the ExPASy server.* Methods Mol Biol, 1999. **112**: p. 531-52.
44. Kwok, S.C. and R.S. Hodges, *Stabilizing and destabilizing clusters in the hydrophobic core of long two-stranded alpha-helical coiled-coils.* J Biol Chem, 2004. **279**(20): p. 21576-88.
45. Provencher, S.W. and J. Glockner, *Estimation of globular protein secondary structure from circular dichroism.* Biochemistry, 1981. **20**(1): p. 33-7.
46. Sreerama, N., S.Y. Venyaminov, and R.W. Woody, *Estimation of the number of alpha-helical and beta-strand segments in proteins using circular dichroism spectroscopy.* Protein Sci, 1999. **8**(2): p. 370-80.
47. Greenfield, N.J., *Using circular dichroism spectra to estimate protein secondary structure.* Nat Protoc, 2006. **1**(6): p. 2876-90.
48. Jackson, M. and H.H. Mantsch, *The use and misuse of FTIR spectroscopy in the determination of protein structure.* Crit Rev Biochem Mol Biol, 1995. **30**(2): p. 95-120.
49. Schneider, C.A., W.S. Rasband, and K.W. Eliceiri, *NIH Image to ImageJ: 25 years of image analysis.* Nature methods, 2012. **9**(7): p. 671-675.
50. Le Droumaguet, B. and K. Velonia, *Click Chemistry: A Powerful Tool to Create Polymer-Based Macromolecular Chimeras.* Macromolecular Rapid Communications, 2008. **29**(12-13): p. 1073-1089.
51. Hong, V., et al., *Electrochemically protected copper(I)-catalyzed azide-alkyne cycloaddition.* Chembiochem, 2008. **9**(9): p. 1481-6.
52. Ishiyama, M., et al., *A highly water-soluble disulfonated tetrazolium salt as a chromogenic indicator for NADH as well as cell viability.* Talanta, 1997. **44**(7): p. 1299-305.
53. Tominaga, H., et al., *A water-soluble tetrazolium salt useful for colorimetric cell viability assay.* Analytical Communications, 1999. **36**(2): p. 47-50.
54. Mascolo, M.C., Y. Pei, and T.A. Ring, *Room Temperature Co-Precipitation Synthesis of Magnetite Nanoparticles in a Large pH Window with Different Bases.* Materials (Basel), 2013. **6**(12): p. 5549-5567.

55. Mérida, F., et al., *Optimization of synthesis and peptization steps to obtain iron oxide nanoparticles with high energy dissipation rates.* J Magn Magn Mater, 2015. **394**: p. 361-371.
56. AXS, B. *DIFFRAC.EVA*. [5] 2020.
57. Vittorio, O., et al., *Multiwall carbon nanotubes as MRI contrast agents for tracking stem cells.* Nanotechnology, 2011. **22**(9): p. 095706.
58. Unterweger, H., et al. *Dextran-coated superparamagnetic iron oxide nanoparticles for magnetic resonance imaging: evaluation of size-dependent imaging properties, storage stability and safety*. International journal of nanomedicine, 2018. **13**, 1899-1915 DOI: 10.2147/ijn.s156528.
59. Corot, C., et al., *Recent advances in iron oxide nanocrystal technology for medical imaging.* Adv Drug Deliv Rev, 2006. **58**(14): p. 1471-504.
60. Janib, S.M., A.S. Moses, and J.A. MacKay, *Imaging and drug delivery using theranostic nanoparticles.* Advanced Drug Delivery Reviews, 2010. **62**(11): p. 1052-1063.
61. Caravan, P., et al., *Influence of molecular parameters and increasing magnetic field strength on relaxivity of gadolinium- and manganese-based T1 contrast agents.* Contrast Media Mol Imaging, 2009. **4**(2): p. 89-100.
62. Pintaske, J., et al., *Relaxivity of Gadopentetate Dimeglumine (Magnevist), Gadobutrol (Gadovist), and Gadobenate Dimeglumine (MultiHance) in human blood plasma at 0.2, 1.5, and 3 Tesla.* Invest Radiol, 2006. **41**(3): p. 213-21.
63. Rohrer, M., et al., *Comparison of magnetic properties of MRI contrast media solutions at different magnetic field strengths.* Invest Radiol, 2005. **40**(11): p. 715-24.
64. Heimburg, T., et al., *FTIR-Spectroscopy of Multistranded Coiled Coil Proteins.* Biochemistry, 1999. **38**(39): p. 12727-12734.
65. Tatulian, S.A., *Structural characterization of membrane proteins and peptides by FTIR and ATR-FTIR spectroscopy.* Methods Mol Biol, 2013. **974**: p. 177-218.
66. Gunasekar, S.K., et al., *Effects of Divalent Metals on Nanoscopic Fiber Formation and Small Molecule Recognition of Helical Proteins.* Advanced Functional Materials, 2012. **22**(10): p. 2154-2159.
67. More, H.T., et al., *Influence of fluorination on protein-engineered coiled-coil fibers.* Biomacromolecules, 2015. **16**(4): p. 1210-7.
68. Gunasekar, S.K., J.S. Haghpanah, and J.K. Montclare, *Assembly of bioinspired helical protein fibers.* Polymers for Advanced Technology, 2008. **19**: p. 454-468.
69. Hong, V., et al., *Analysis and optimization of copper-catalyzed azide-alkyne cycloaddition for bioconjugation.* Angew Chem Int Ed Engl, 2009. **48**(52): p. 9879-83.
70. Hachani, R., et al., *Assessing cell-nanoparticle interactions by high content imaging of biocompatible iron oxide nanoparticles as potential contrast agents for magnetic resonance imaging.* Sci Rep, 2017. **7**(1): p. 7850.
71. Swain, P. and S.K. Srivastava, *Exploring quantum Griffiths phase in Ni(1-x) V (x) nanoalloys.* Sci Rep, 2017. **7**(1): p. 1223.
72. Bragg, W.H., *The Structure of Magnetite and the Spinels.* Nature, 1915. **95**(2386): p. 561-561.
73. Bragg, W.H., *The Nature of γ and X-Rays.* Nature, 1908. **77**(1995): p. 270-271.

74. Pauling, L. and S.B. Hendricks, *THE CRYSTAL STRUCTURES OF HEMATITE AND CORUNDUM.* Journal of the American Chemical Society, 1925. **47**(3): p. 781-790.
75. Burtea, C., et al., *Contrast agents: magnetic resonance.* Handb Exp Pharmacol, 2008(185 Pt 1): p. 135-65.
76. Fasano, M., et al., *The extraordinary ligand binding properties of human serum albumin.* IUBMB Life, 2005. **57**(12): p. 787-96.
77. Taira, Z. and H. Terada, *Specific and non-specific ligand binding to serum albumin.* Biochem Pharmacol, 1985. **34**(11): p. 1999-2005.
78. Yang, R., et al., *Preparation of folic acid-conjugated, doxorubicin-loaded, magnetic bovine serum albumin nanospheres and their antitumor effects in vitro and in vivo.* Int J Nanomedicine, 2014. **9**: p. 4231-43.
79. Kashyap, S., et al., *Nucleation of iron oxide nanoparticles mediated by Mms6 protein in situ.* ACS Nano, 2014. **8**(9): p. 9097-106.
80. Shapiro, E.M., *Biodegradable, polymer encapsulated, metal oxide particles for MRI-based cell tracking.* Magn Reson Med, 2015. **73**(1): p. 376-89.
81. Antal, I., et al., *MRI Relaxivity Changes of the Magnetic Nanoparticles Induced by Different Amino Acid Coatings.* Nanomaterials, 2020. **10**(2).
82. Granot, D. and E.M. Shapiro, *Release activation of iron oxide nanoparticles: (REACTION) a novel environmentally sensitive MRI paradigm.* Magn Reson Med, 2011. **65**(5): p. 1253-9.
83. Perez, J.M., L. Josephson, and R. Weissleder, *Use of magnetic nanoparticles as nanosensors to probe for molecular interactions.* Chembiochem, 2004. **5**(3): p. 261-4.
84. Bowen, C.V., et al., *Application of the static dephasing regime theory to superparamagnetic iron-oxide loaded cells.* Magnetic resonance in medicine, 2002. **48**(1): p. 52-61.
85. Weisskoff, R.M., et al., *Microscopic susceptibility variation and transverse relaxation: theory and experiment.* Magnetic resonance in medicine, 1994. **31**(6): p. 601-610.
86. Chavhan, G.B., et al., *Principles, Techniques, and Applications of T2*-based MR Imaging and Its Special Applications.* RadioGraphics, 2009. **29**(5): p. 1433-1449.
87. Jun, Y.W., et al., *Nanoscale size effect of magnetic nanocrystals and their utilization for cancer diagnosis via magnetic resonance imaging.* J Am Chem Soc, 2005. **127**(16): p. 5732-3.